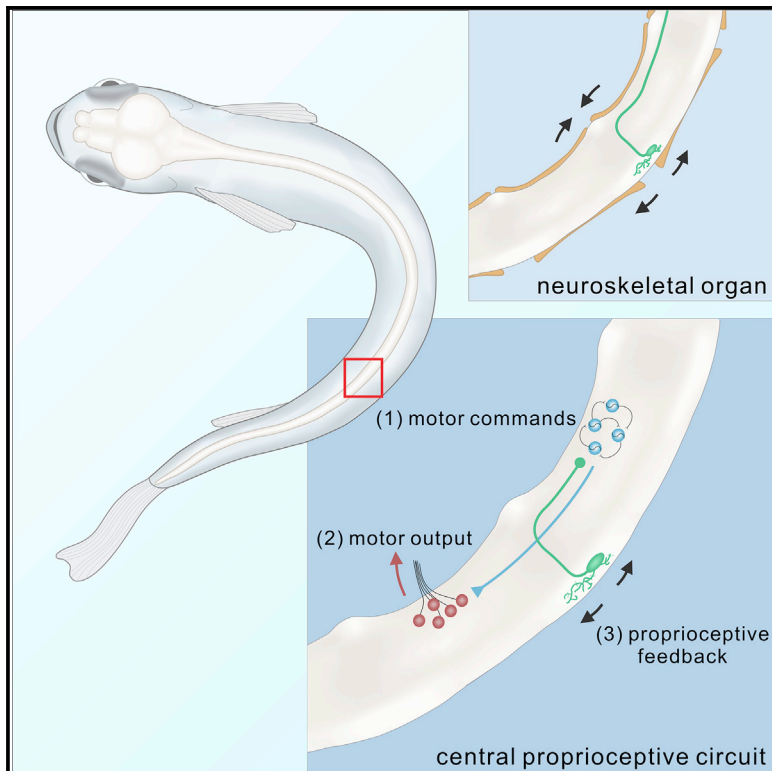# A spinal organ of proprioception for integrated motor action feedback

Graphical Abstract

Authors

Laurence D. Picton, Maria Bertuzzi, Irene Pallucchi, ...,
Francesco Iacoviello, Paul R. Shearing,
Abdeljabbar El Manira

Correspondence

abdel.elmanira@ki.se

In Brief

Picton et al. reveal a central organ of proprioception embedded with Piezo2-expressing mechanosensitive neurons in adult zebrafish. These neurons are endowed with a hybrid function as sensory neurons and commissural inhibitory neurons, merging proprioceptive feedback and locomotor rhythm generation into a unified sensorimotor circuit.

Highlights

- A central organ of proprioception exists in the spinal cord

- Piezo2-expressing mechanosensitive neurons sense lateral bending of spinal cord

- These are inhibitory commissural neurons targeting the locomotor rhythm generator

- Intraspinal proprioceptive feedback aligns movements with motor commands

Neuron

CellPress
OPEN ACCESS

Article

A spinal organ of proprioception for integrated motor action feedback

Laurence D. Picton,[1] Maria Bertuzzi,[1] Irene Pallucchi,[1] Pierre Fontanel,[1] Elin Dahlberg,[1] E. Rebecka Björnfors,[1] Francesco Iacoviello,[2] Paul R. Shearing,[2] and Abdeljabbar El Manira[1,3,*]

[1]Department of Neuroscience, Karolinska Institutet, 171 77 Stockholm, Sweden
[2]Electrochemical Innovation Lab, Department of Chemical Engineering, University College London, London, UK
[3]Lead contact
*Correspondence: abdel.elmanira@ki.se
https://doi.org/10.1016/j.neuron.2021.01.018

SUMMARY

Proprioception is essential for behavior and provides a sense of our body movements in physical space. Proprioceptor organs are thought to be only in the periphery. Whether the central nervous system can intrinsically sense its own movement remains unclear. Here we identify a segmental organ of proprioception in the adult zebrafish spinal cord, which is embedded by intraspinal mechanosensory neurons expressing Piezo2 channels. These cells are late-born, inhibitory, commissural neurons with unique molecular and physiological profiles reflecting a dual sensory and motor function. The central proprioceptive organ locally detects lateral body movements during locomotion and provides direct inhibitory feedback onto rhythm-generating interneurons responsible for the central motor program. This dynamically aligns central pattern generation with movement outcome for efficient locomotion. Our results demonstrate that a central proprioceptive organ monitors self-movement using hybrid neurons that merge sensory and motor entities into a unified network.

INTRODUCTION

The primacy of movement in all animal behavior is reflected by diverse neural circuits and sensory organs dedicated to control of motor actions (Arber and Costa, 2018; Brownstone and Bui, 2010; Brownstone and Wilson, 2008; Goulding, 2009; Grillner and El Manira, 2020; Kiehn, 2016; Orlovsky et al., 1999). To move effectively, all animals need a reliable sense of their own movement, and proprioception provides essential real-time feedback on body position in physical space (the so-called "sixth sense"). The accepted view is that this sense is afforded entirely by peripheral proprioceptors embedded in proprioceptive organs in muscles, tendons, and joints. However, it is possible that central proprioceptor organs may also exist and directly monitor movement of the central nervous system (CNS) itself.

In vertebrates, including humans, it is well established but often overlooked that the brainstem and spinal cord undergo significant distortions in shape during normal body movements that depend on the direction and amplitude of a motor action (Breig, 1960; Harrison et al., 1999; Rossitti, 1993). Changes in the shape and tension of the CNS itself therefore encode information that could be integrated as feedback to guide behavior (Grillner, 1986; Grillner and Wallén, 1982). A central sensory mechanism for detecting such a signal has been described previously only in lampreys, which are the only vertebrate that lack a bony skel-

eton but have stretch-sensitive neurons along the lateral margins of their highly flexible spinal cord (Di Prisco et al., 1990; Grillner et al., 1984; McClellan and Sigvardt, 1988). It remains unclear how, in the presence of a stabilizing vertebral column, a mechanism of central proprioception could function or how this feedback could influence motor circuits controlling behavior. Nevertheless, in all bony vertebrates, distortions of neural tissue are primarily focused at the lateral edges of intervertebral spinal cord regions, where bones, ligaments, and CNS soft tissue interact.

Across vertebrates, there is anatomical evidence of neurons with unknown function and origin located at the lateral margins of the CNS (Anadón et al., 1995; Anderson, 1963; Anderson et al., 1964; Donald, 1953; Fernández et al., 1998; Li et al., 2020; Necker, 2006; Schroeder and Egar, 1990; Schroeder, 1986; Sherrington, 1890). In mammals, including cats, monkeys, and humans, these neurons are segmentally aggregated in the spinal cord at the attachment site of suspensory dentate ligaments, which are known to transfer tension directly to this region during movement of the body (Anderson, 1963; Anderson et al., 1964; Ceylan et al., 2012; Donald, 1953; Harrison et al., 1999). Despite strong and broad evidence across vertebrates of continuous changes in shape and tension of CNS tissue during behavior, no studies have directly tested the novel hypothesis that there are central proprioceptive organs for monitoring the position and movement of the brain and spinal cord.
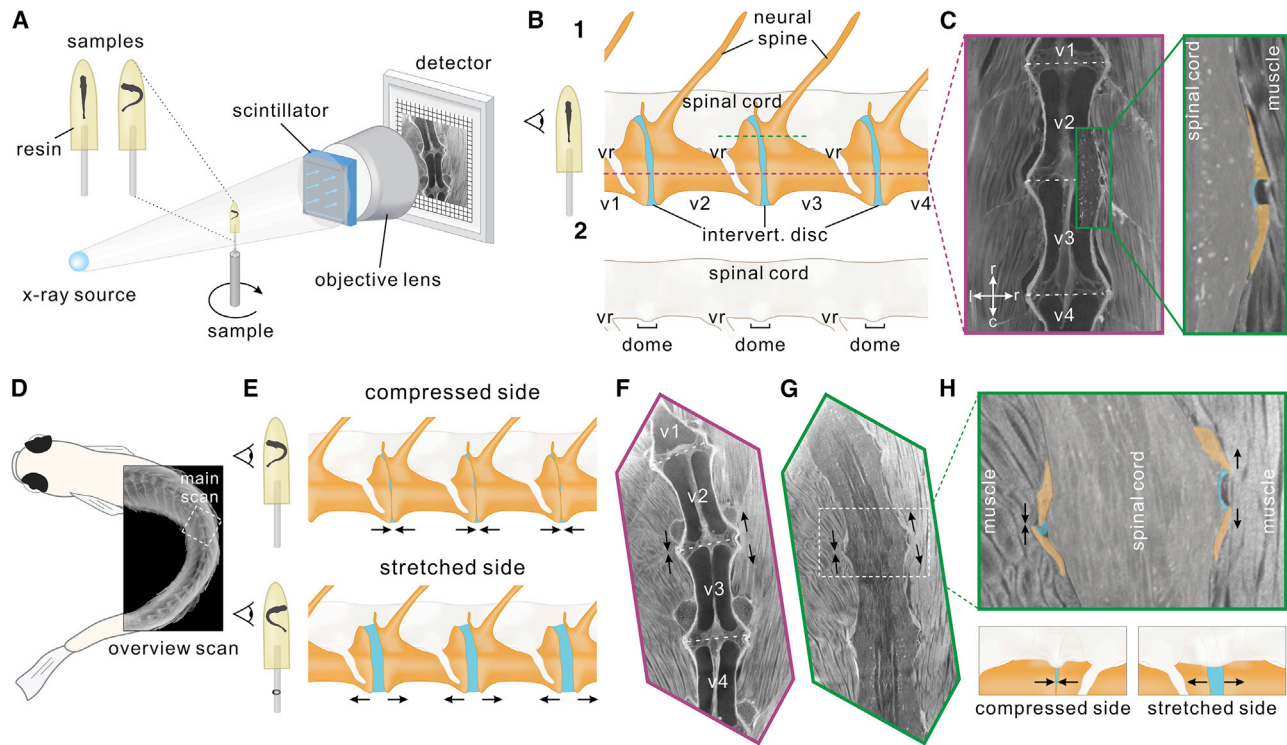
Figure 1. A neuroskeletal organ affected by movement of the intervertebral joints

(A) Schematic of the micro-CT scan method.

(B1) Schematic of three intervertebral regions, showing the arrangement of bones (orange), intervertebral discs (blue), and spinal cord (white) in adult zebrafish. Dashed colored lines indicate the level of the raw images shown in (C).

(B2) Schematic of the spinal cord, showing ventrolateral enlargements ("dome") located at each intervertebral region.

(C) Raw micro-CT scan image showing three intervertebral regions. The green box is an overlay of an image at the level of the spinal cord, showing a single dome. An expansion of this region is shown, with the bones, intervertebral disc, and spinal cord highlighted.

(D) Schematic and raw images of a curved fish in which approximately three intervertebral joints were scanned.

(E) Neuroskeletal architecture on the stretched and compressed side of a curved fish.

(F) Raw images of a curved fish at the level of the vertebrae, showing the stretched and compressed sides.

(G) Raw images at the level of the spinal cord domes, which are compressed on one side and stretched laterally on the other side.

(H) Expansion of a single intervertebral region, with the spinal cord, bone, and intervertebral disc highlighted. Shown below is a schematic of a single spinal cord dome on the stretched and compressed sides in a curved fish.

In this study, we reveal a novel spinal proprioceptor organ in the adult zebrafish and demonstrate that it functions as a sensorimotor servomechanism to optimize movement for efficient locomotion. This organ is formed by segmental enlargements of the lateral spinal cord that are permeated by a specialized class of late-born and centrally derived mechanosensitive neurons with unique molecular profiles. These intraspinal proprioceptors act with a dual sensorimotor function. They express mechanosensitive Piezo2 channels that allow them to gauge local distortions of spinal tissue occurring at the intervertebral region during body bending. At the same time, intraspinal proprioceptors are also ingrained in the central motor program and exert direct, inhibitory control over the rhythm-generating circuit for efficient locomotor movements *in vivo*. Thus, the central circuit revealed here forms an elegant hybrid model of sensorimotor processing that merges central pattern generation and proprioception into a single network entity.

RESULTS

A neuroskeletal sensory organ

Locomotion in fish involves lateral body undulations that cause small displacements of individual vertebrae along the spinal column, generating localized strain at each intervertebral region. This biological signal could be sensed by specialized structures located in the spinal cord. To determine whether such a structure exists, we performed a micro-computed tomography (micro-CT) scan (Figure 1A) of several segments of adult zebrafish, providing a high-resolution overview of the neuroskeletal architecture in the intact animal. At the region of each intervertebral disc (Figure 1B, blue), we identified a ventrolateral enlargement (dome) of spinal cord tissue located under a pouch formed by protruding bones of consecutive vertebrae, connected by the flexible intervertebral disc (Figures 1B and 1C). We next imaged a zebrafish fixed in a curved position, mimicking body bending during swimming (Figure 1D). Consecutive vertebrae were
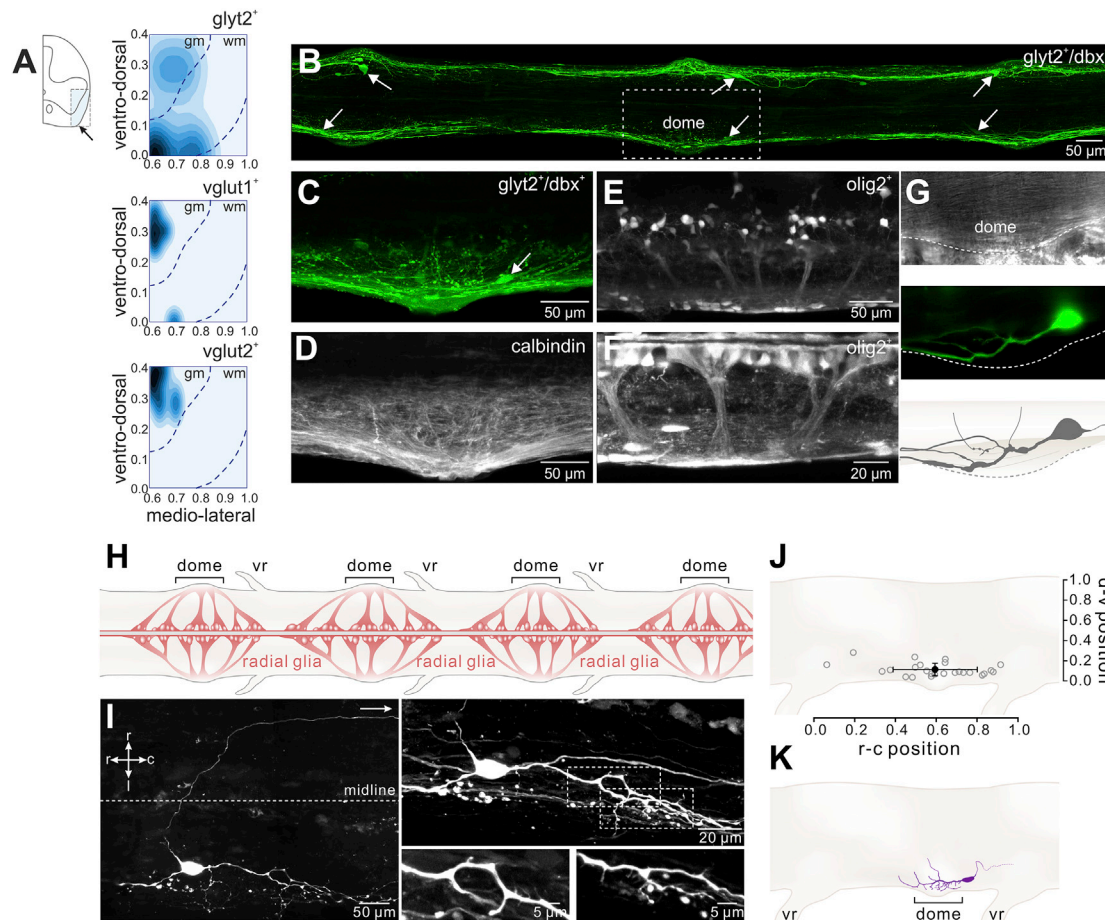
Figure 2. Lateral spinal cord enlargements are embedded with specialized inhibitory neurons

(A) Density distribution of neuron soma positions in the ventrolateral spinal cord of three lines of transgenic zebrafish (*glyt2*[+], *vglut1*[+], and *vglut2*[+]). wm, white matter; gm, gray matter; ~15 segments from 4 fish in each transgenic line: *Tg(glyt2:GFP)*, *Tg(vglut1hs:GFP)*, and *Tg(vglut2a:LOXP-DsRed-LOXP-GFP)*.

(B) Overview of confocal images showing three spinal cord domes (spinal segments 13, 14, and 15) on either side of the spinal cord in *Tg(dbx1b:Cre)* × *Tg(glyt2:LOXP-DsRed-LOXP-GFP)* zebrafish, labeling *glyt2*[+]/*dbx1b*^{+} neurons (white arrows).

(C) Expansion of a single spinal cord dome (segment 14), showing a glycinergic neuron located close to the dome.

(D) Confocal image showing *Calbindin* expression in the spinal cord dome (segment 14).

(E) Confocal images showing *olig2*[+] radial projections from the central canal to the spinal cord dome (segment 14).

(F) An expanded image of *olig2*[+] radial projections (segment 14).

(G) Top: charge-coupled device (CCD) camera image of the spinal cord dome. Center: GFP expression of a single *glyt2*[+]/*dbx1b*[+] neuron whose projections are embedded in the dome. Bottom: morphological reconstruction of the *glyt2*[+]/*dbx1b*[+] neuron in the dome.

(H) Schematic of segmental radial glia projections from the central canal to the spinal cord domes, as identified using *olig2* expression.

(I) Overview of confocal images of a neurobiotin-filled lateral glycinergic neuron. The dendrites of the neuron project laterally, whereas its axon crosses the spinal cord and ascends on the opposite side. An expansion of the dendrites shows fine spicular processes emanating from the lateral dendrites at the level of the spinal cord dome.

(J) Position of lateral glycinergic neuron somata within the spinal cord, which were distributed at the ventrolateral edge, close to the spinal cord dome within segments (n = 25 lateral neurons).

(K) An example of a neurobiotin-filled lateral neuron with projections in the spinal cord dome.

moved closer together on the compressed side, whereas they were pulled apart, stretching the intervertebral disc, on the opposite side (Figures 2E and 2F). This was translated into an asymmetrical distortion of spinal cord domes on either side of the body, which was stretched laterally on the open side (Figures 1G and 1H; Video S1). This demonstrates that, during each body bend, segmental spinal domes are subjected to lateralized changes in shape and tension at each intervertebral region.

To detect this stretch, neurons would need to be located in or around the spinal dome in the ventrolateral white matter. We examined the soma position of neurons in the spinal cord in three transgenic zebrafish lines, broadly labeling excitatory and inhibitory neurons. We identified a population of inhibitory glycinergic neurons in the ventrolateral margins of the white matter (Figure 2A), whereas excitatory glutamatergic neurons were restricted to the gray matter (Figure 2A). These glycinergic
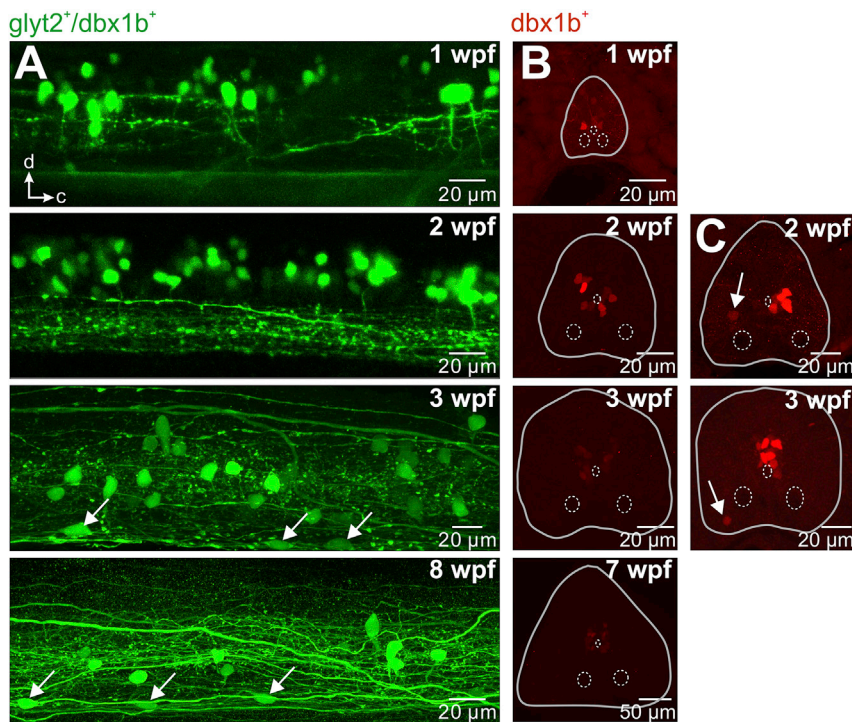
Neuron
Article

glyt2⁺/dbx1b⁺   dbx1b⁺

Figure 3. Lateral neurons appear 3 weeks into development and are derived from progenitors at the central canal

(A) Maximum intensity confocal images of 1–2 segments of spinal cord from *Tg(glyt2,dbx:GFP)* zebrafish, showing GFP expression in *glyt2⁺/dbx1b⁺* neurons at different stages of development (fish length: 5, 7, 9, and 18 mm, respectively). Lateral *glyt2⁺/dbx1b⁺* neurons (white arrows) appeared in the spinal cord approximately 3 weeks post fertilization (wpf; 9 mm).

(B) *Dbx1b* expression at different stages of development in *Tg(dbx1b:Cre)* zebrafish. There is a transient increase in expression of *dbx1b* at approximately 2 wpf (7 mm) in development. The dashed white circles indicate the position of the central canal and Mauthner axons.

(C) 2 and 3 wpf, a number of *dbx1b⁺* neurons (white arrows) were located in a position ventrolateral to the central canal, toward the spinal cord domes.

neurons also expressed the transcription factor Dbx1b and were repeated segmentally close to the spinal dome (Figures 2B, 2C, 2J, and 2K; 1.2 ± 0.8 cells per hemisegment, n = 6 fish). This dome is a defined structure with a scaffold of radial projections from the central canal that express the calcium-binding protein Calbindin and Olig2, which is known to label radial glia and oligodendrocyte-lineage cells (Berg et al., 2018; Park et al., 2007; Stil and Drapeau, 2016; Figures 2D–2F and 2H). Furthermore, glycinergic *dbx1b⁺* neurons showed extensive, fine dendritic projections that permeated the dome and had a commissural, ascending axon (Figures 2G and 2I).

These prominent glycinergic *dbx1b⁺* neurons were absent in larval zebrafish and appeared only around 2–3 weeks into development (Figure 3A). At this time point, there was increased expression of *dbx1b* in cells surrounding the central canal, where radial glia cells are located, suggesting a late wave of neuronal proliferation (Figure 3B). 2–3 weeks into development, a number of these *dbx1b⁺* neurons were separated from the cluster at the central canal and were located in a position close to the spinal dome (Figure 3C).

These results show that the spinal cord has segmental enlargements located at each intervertebral region that are subject to stretch during movement and contain late-born inhibitory commissural neurons. This structure may be a specialized neuroskeletal sensory organ.

Molecular profiling reveals specialized intraspinal proprioceptor neurons

To examine the molecular identities of the neurons in this specialized organ, we used single-cell RNA sequencing (scRNA-seq) of the *glyt2⁺/dbx1b⁺* population in the spinal cord (Figures 4A and 4B). Using clustering analysis of *glyt2⁺/dbx1b⁺* cells sorted by fluorescence-activated cell sorting (FACS), we obtained 6 separate clusters of cells (Figure 4C). Two of these clusters (neuronal cluster 1 [n_1] and 2 [n_2]) expressed pan-neuronal markers, vesicular inhibitory amino acid transporters, and synaptic markers (Figures 4C and 4D), whereas the other four expressed markers of glial subtypes (g_1–g_4; Figure 4C). To determine which of the two neuronal clusters corresponds to neurons located in the white matter close to the spinal dome, we used a modified patch-seq method to harvest single *glyt2⁺/dbx1b⁺* neurons from this region and compared their gene profiles with each of the clusters (Figures 4B and 4E). The gene profile of lateral *glyt2⁺/dbx1b⁺* neurons showed a high-percentage overlap with n_1, and 21 of 22 of the neurons were assigned the identity of cluster n_1 (Figures 4E and S1). Conversely, the gene profile of single *glyt2⁺/dbx1b⁺* neurons collected from the gray matter overlapped mostly with n_2 (Figure 4F). The latter neurons correspond to the V0d interneuron population described previously in this zebrafish line (Satou et al., 2012, 2020). We therefore performed a more detailed analysis of n_1 corresponding to the lateral neurons of the spinal enlargements.

Our scRNA-seq analysis revealed that several genes were differentially expressed in this population (Figures 4G and 4H). Importantly, n_1 neurons were significantly enriched in genes encoding mechanosensitive channels, including *piezo2*, *tmem63c*, *tmem63bb*, and *asic2* (Coste et al., 2010, 2012; Murthy et al., 2018; Ranade et al., 2015), as well as genes associated with sensory response termination and adaptation, such as *kcna1a* and *slc24a4b* (Hao et al., 2013; Stephan et al., 2011; Figure 4I). Furthermore, these neurons were also significantly enriched in genes associated with a late-born, radial glia-derived neuronal profile (Lange et al., 2020; Figure 4J) as well as a number of genes related to cilium function and development, including *spa17* (Grizzi et al., 2004; Figure 4K). Finally, we also identified
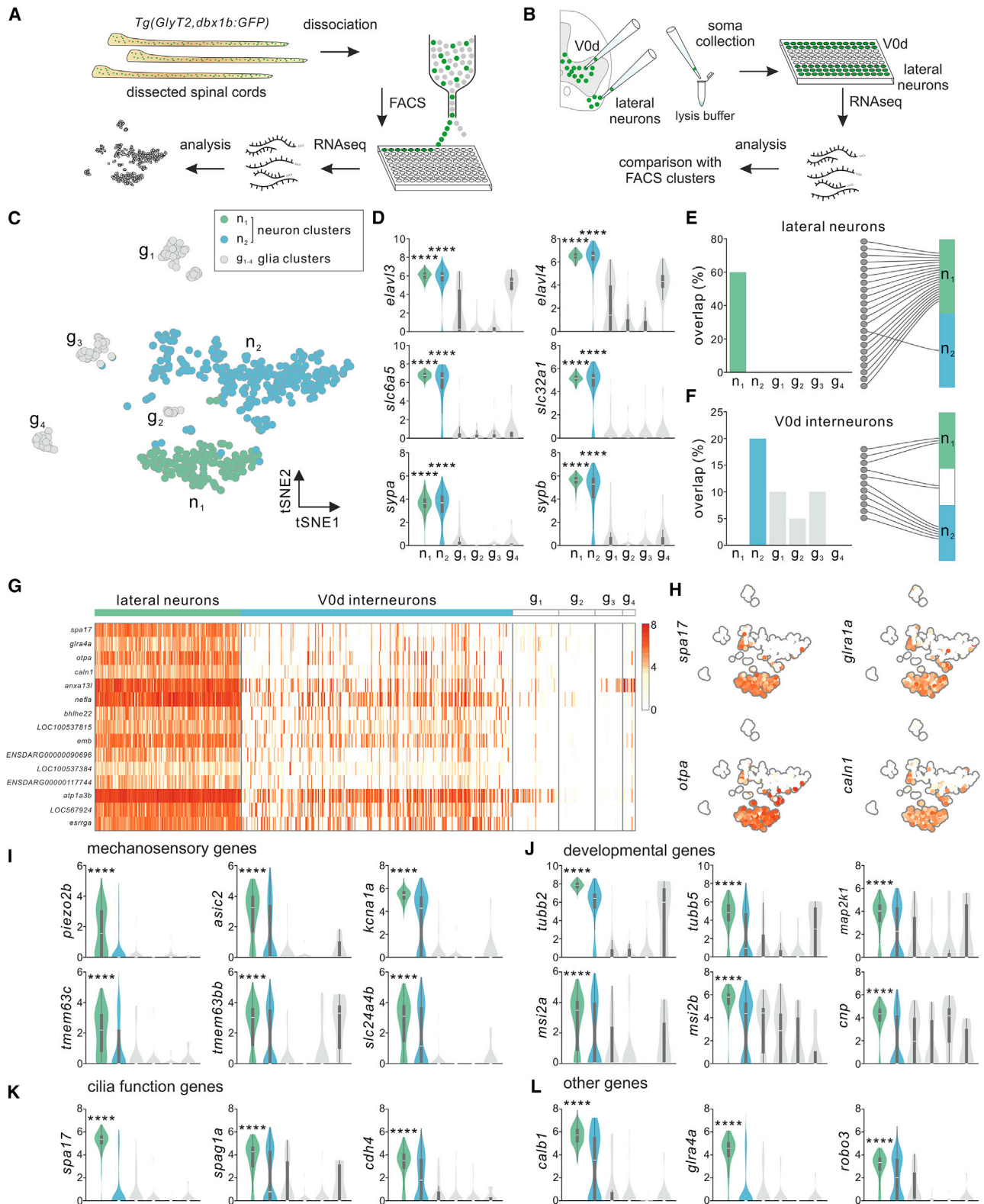
Figure 4. Deep single-cell RNA-seq (scRNA-seq) of *glyt2*[+]/*dbx1b*^{+} cells reveals spinal commissural neurons with sensory function

(A) Overview of the single-cell sequencing pipeline. Spinal cords from *Tg(glyt2,dbx:GFP)* zebrafish (n = 32 fish) labeling *glyt2*[+]/*dbx1b*^{+} cells were dissected, dissociated, and sorted by FACS to obtain GFP-positive neurons. Single-neuron mRNA was then sequenced using Smart-seq2, filtered, and analyzed.

(legend continued on next page)

a number of other functionally relevant genes enriched in lateral spinal cord neurons, including *calbindin*, *glra4a*, and *robo3*, with the latter involved in guidance of midline axonal crossing of commissural neurons (Chen et al., 2008; Friocourt and Chédotal, 2017; Sabatier et al., 2004; Figure 4L).

These results indicate that the neurons embedded in segmental spinal cord domes have the unique molecular profiles of mechanosensitive, late-born, commissural inhibitory neurons. This suggests that this structure may be a specialized intraspinal lateral proprioceptor (ILP) organ.

Piezo2-mediated mechanotransduction at the lateral proprioceptor organ

Piezo2 proteins are mechanosensitive ion channels involved in proprioception (Coste et al., 2010, 2012; Murthy et al., 2017; Woo et al., 2015). Selective expression of *piezo2* by ILP neurons was validated using an *in situ* hybridization method (RNAscope) in adult zebrafish expressing GFP in $glyt2^+/dbx1b^+$ neurons. There was strong and selective expression of *piezo2* in $glyt2^+/dbx1b^+$ ILP neurons (Figures 5A–5C, S2C, and S2E), whereas virtually no *piezo2* expression was detected in V0d interneurons (Figures 5C and S2A–S2E). Furthermore, at early developmental stages (zebrafish 2 days post fertilization [dpf]), expression of *piezo2* was restricted to dorsally located Rohon-Beard sensory neurons (Faucherre et al., 2013; Figure S2F), consistent with late development of the ILP population.

Piezo2-mediated mechanosensation in $glyt2^+/dbx1b^+$ ILP neurons was functionally validated using mechanoclamp recordings. Brief and rapid mechanical indentations of the ILP neuron soma induced mechanically activated inward currents (MA currents) (Figure 5D), whereas no responses were observed in control motor neurons and V0d interneurons (Figures S3A and S3B). The MA current in ILP neurons was proportional to the amplitude of the mechanical stimulation, was rapidly inactivating (mean tau of inactivation, 8.9 ± 1.7 ms), and was blocked by ruthenium red, a known blocker of Piezo channels (Coste et al., 2012; Figure 5E). We next tested how ILP neurons encode a more physiological mechanical stimulus. Locally stretching the spinal cord at the level of the ILP organ produced a depolarization in ILP neurons that was graded to the amplitude and velocity of the stimulus

and triggered trains of action potentials (Figures 5F, S4A, and S4B). These responses occurred only to spinal cord stretch and not to compression (Figure S3C), and no responses to spinal cord stretch were observed in control motor neurons or V0d interneurons (Figure S3D). Furthermore, ILP neurons displayed low-threshold firing properties and displayed only small, sub-threshold oscillations of the membrane potential during centrally generated locomotor activity in the absence of movement. These oscillations were phase delayed relative to the ipsilateral ventral root recordings (mean phase value, 0.10 ± 0.03; n = 5 cells from 4 fish) (Figures S4C–S4G).

These results show that ILP neurons are endowed with properties of low-threshold mechanosensitivity, enabling them to dynamically encode local distortions of the spinal cord and act as intraspinal proprioceptors.

ILP neurons provide commissural inhibitory feedback on movement

ILP neurons have molecular profiles of proprioceptors and inhibitory commissural neurons. Morphological analysis confirmed that their axons crossed the midline and projected rostrally over many segments along the ventrolateral aspect of the spinal cord (Figure 6A), making close contact with ILP neurons on the opposite side (Figure 6B). The existence of direct synaptic connections was confirmed using dual whole-cell patch-clamp recordings. Consistent with their rostral axon projection, unidirectional inhibitory postsynaptic potentials (IPSPs) were elicited only in rostral contralateral ILP neurons (Figure 6C) and were blocked by a combination of glycine and GABA_A receptor antagonists (Figure 6D). This unidirectional commissural inhibition among ILP neurons was also elicited by mechanical stimulation of these proprioceptors, induced by lateral bending of the isolated spinal cord that mimicked natural movements during swimming (Figure 6E). An important functional consequence of this inhibition is direct and reliable control of firing of the proprioceptors on the opposite side, as confirmed by silencing of spiking following unidirectional bending (Figure 6F). This movement-related commissural inhibition was also induced by locally stretching a contralateral ILP organ (Figure 6G) and was blocked by a combination of glycine and GABA_A receptor antagonists (Figure 6H), demonstrating

---

(B) Overview of the modified patch-seq pipeline. Based on their position in the spinal cord, single lateral neurons and V0d interneurons were harvested using a patch pipette. Single-neuron mRNA was then sequenced using Smart-seq2, filtered, and analyzed.

(C) tSNE plot of the $glyt2^+/dbx1b^+$ population (n = 550 cells after quality control and filtering). Principal-component analysis (PCA) of single-cell gene expression revealed two neuronal clusters (n_1 and n_2) and 4 glial clusters (g_1–g_4).

(D) Violin plots showing normalized gene expression levels for inhibitory interneuron marker genes. n_1 and n_2 were enriched significantly in genes encoding pan-neuronal markers (*elavl3/4*), GABA/glycine transporters (*slc6a5* and *slc32a1*), and synaptic markers (*sypa/b*).

(E) Left: overlap between enriched genes in anatomically identified lateral neurons and each population cluster. Right: SCmap analysis assigned the identity of 21 of 22 lateral neurons to the molecular profile of n_1.

(F) Left: gene profiles of anatomically identified V0d interneurons overlapped mostly with the profile of n_2. Right: SCmap analysis assigned the identity of 6 of 11 V0d interneurons to the molecular profile of n_2 and 3 of 11 to n_1, and 2 of 11 were unassigned.

(G) Heatmap of the most significantly enriched genes in n_1 (lateral neurons).

(H) tSNE cluster plots of the $glyt2^+/dbx1b^+$ population, with each cell colored according to the expression of a number of key marker genes for lateral neurons.

(I) Violin plots showing normalized expression levels for a range of genes enriched significantly in lateral neurons that encode mechanosensitive channels and channels associated with sensory response termination (****$p < 0.0001$).

(J) Violin plots of a range of genes shown previously in adult zebrafish as marker genes for newborn neurons derived from late proliferation of radial glia (****$p < 0.0001$).

(K) Violin plots of a range of genes associated with cilium development and function (****$p < 0.0001$).

(L) Violin plots for a range of functionally relevant genes, including genes associated with calcium binding (*calb1*), commissural axon guidance (*robo3*), and a glycine receptor subtype (*glra4a*) that was absent in V0d interneurons (****$p < 0.0001$).
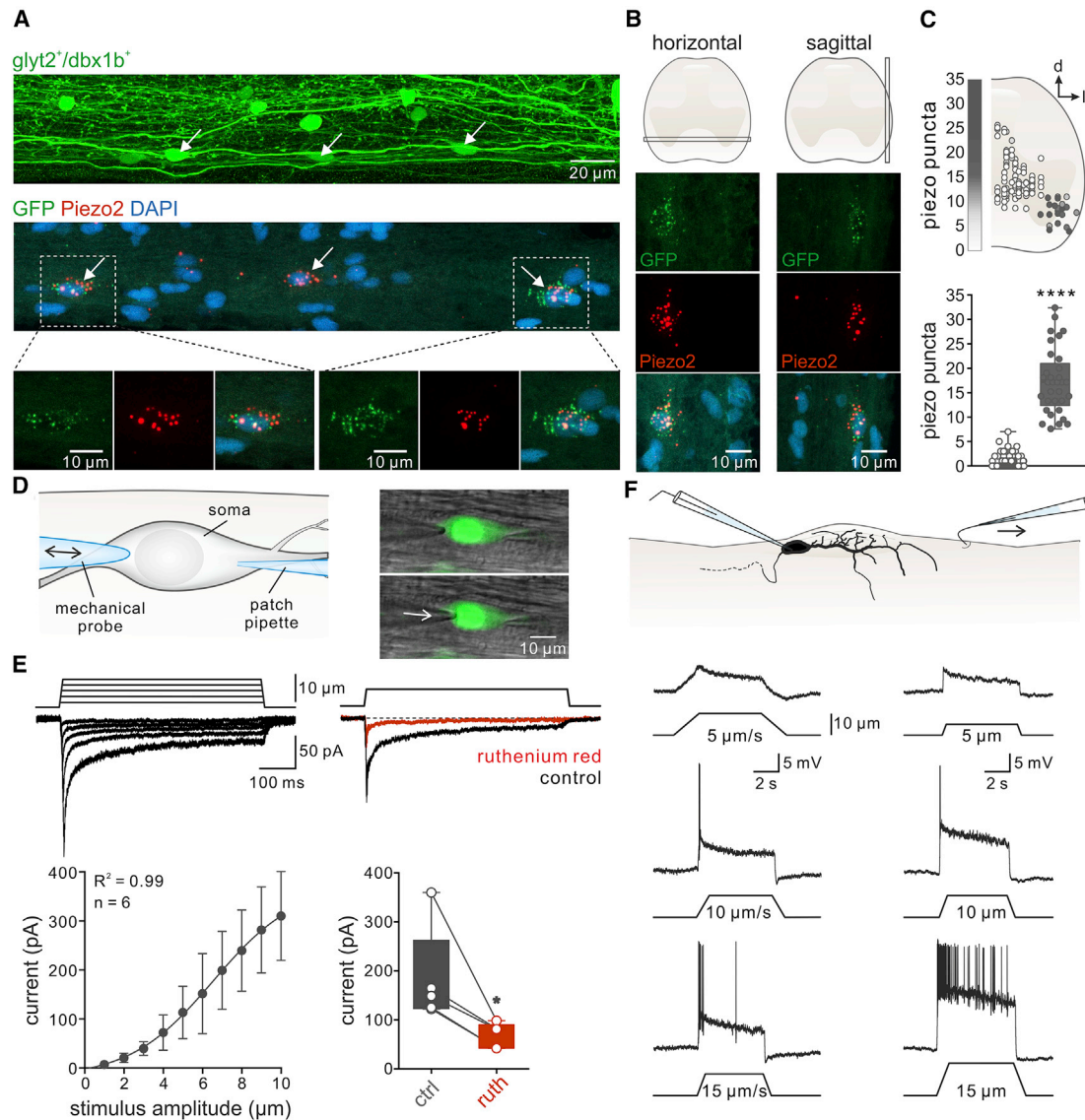
Figure 5. Intraspinal lateral mechanosensory neurons encode spinal cord movement

(A) Top: maximum-intensity confocal projection of ventral spinal cord from *Tg(glyt2,dbx:GFP)* fish, highlighting three ILP neurons at the ventral edge. Center: representative image of three ILP neurons following an RNAscope multiplex fluorescence assay, showing expression of *piezo2* and GFP RNA, with nuclei stained using DAPI. An enlarged view of two ILP neurons is shown below, showing GFP and *piezo2* RNA puncta.

(B) Two further examples (one horizontal and one sagittal section) of GFP-positive ILP neurons enriched in RNA puncta for *piezo2*.

(C) Distribution of the soma position of GFP-positive *glyt2*[+]/*dbx*^{+} neurons, colored according to the number of *piezo2* RNA puncta. *Piezo2* RNA expression was restricted to lateral neurons compared with V0d interneurons (****$p < 0.0001$, n = 33 lateral neurons and 276 V0d interneurons from 4 fish).

(D) Mechanoclamp technique, in which a blunt mechanical probe is used to make brief indentations of the neuron soma while making a patch-clamp recording. Right: an image of a GFP-positive ILP neuron during a recording, before and after the probe was moved 5 μm into the soma.

(E) Voltage-clamp recordings showing mechanically activated (MA) currents in response to indentation of the soma in a range of 1–10 μm (n = 6 cells from 4 fish, error bars represent standard deviation). MA currents were rapidly inactivating and blocked significantly by 50 μm ruthenium red (*$p < 0.05$, n = 5 cells from 5 fish).

(F) Schematic of the local spinal cord organ stretch experiments. The projections of a single ILP neuron were stretched while making a patch-clamp recording in current-clamp mode. Shown below are raw recording traces of an ILP neuron in response to stretch of the ventrolateral margin of the spinal cord with increased amplitude or velocity.

that they act through a combination of GABA and glycine. Furthermore, ablation of ILP neurons on the stretched side virtually abolished the inhibitory responses to bending in contralateral ILP neurons (Figures S3E–S3G).

These results show that ILP neurons act not only as proprioceptors but also as movement-coupled inhibitory commissural neurons that transform spinal cord movements into a negative feedback signal.
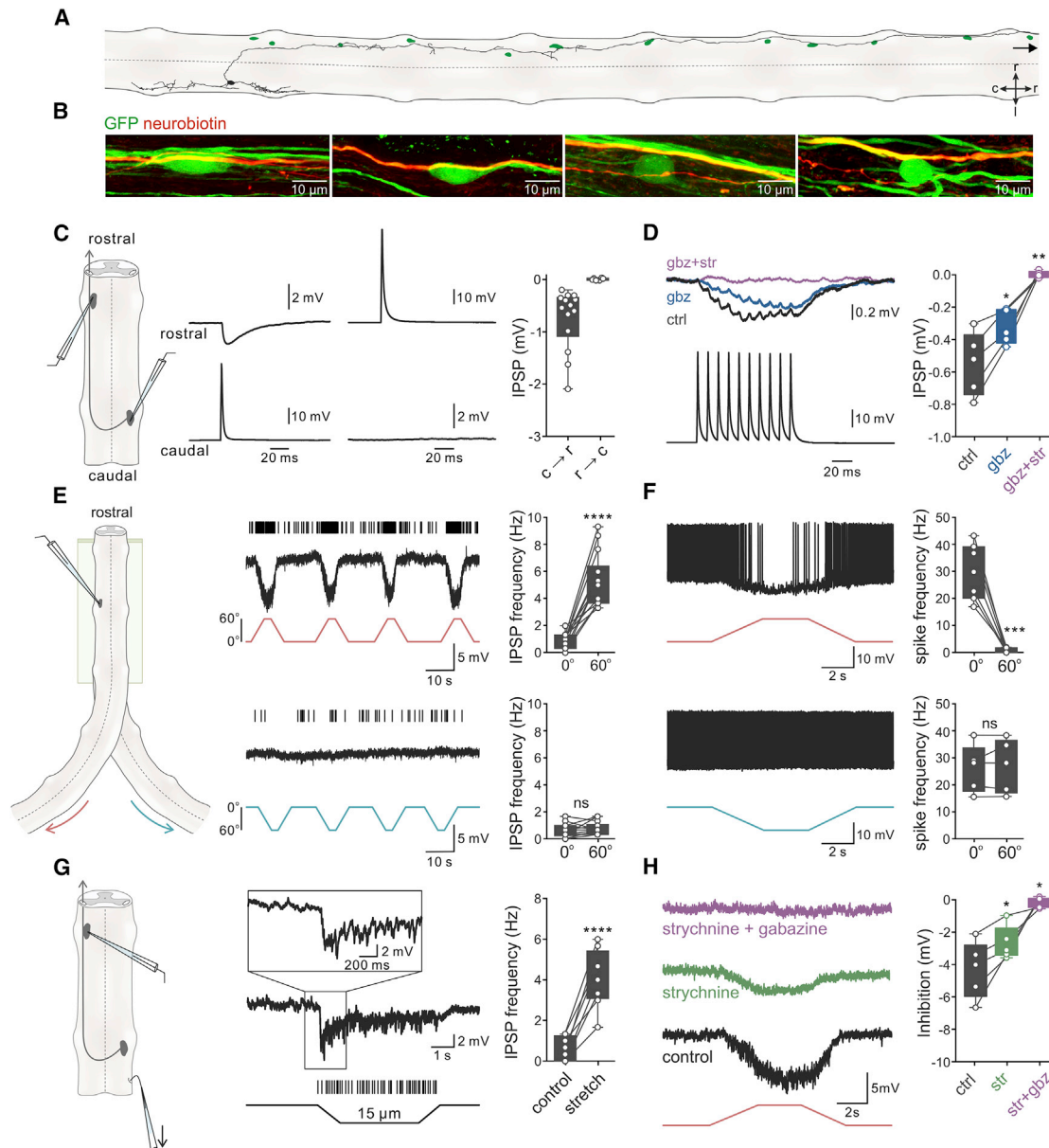
Figure 6. ILP neurons provide rostral inhibition to contralateral ILP neurons

(A) Schematic of the spinal cord (ventral side up), showing a reconstruction of a neurobiotin-filled ILP neuron, its axon crossing the midline and making contact with rostral, contralateral ILP neurons.

(B) Examples of contacts between a single neurobiotin-filled ILP neuron and contralateral ILP neurons.

(C) Single action potentials in a caudal ILP neuron induced an IPSP in a simultaneously recorded rostral ILP neuron (n = 14 pairs tested from 14 fish) but not in the opposite direction (n = 6 pairs tested from 6 fish).

(D) The IPSPs were blocked by a combination of GABAzine (10 μM) and strychnine (5 μM) (*p < 0.05, **p < 0.01, n = 5 pairs from 5 fish).

(E) Bending the spinal cord to stretch the contralateral side produced IPSPs (vertical lines) in a rostrally located ILP neuron (****p < 0.0001, n = 14 cells from 9 fish), whereas bending the spinal cord to stretch the ipsilateral side induced no response (p > 0.05, n = 14 cells from 9 fish).

(F) Inhibitory responses induced by bending to stretch the contralateral side were sufficient to silence spiking in ILP neurons induced by a depolarizing current injection (***p < 0.001, n = 7 cells from 5 fish). Bending in the opposite direction had no effect on spiking (p > 0.05, n = 6 cells from 5 fish).

(G) Local stretch of a contralateral ILP neuron was sufficient to induce inhibitory responses (vertical lines) in a rostral ILP neuron (****p < 0.0001, n = 8 cells from 6 fish).

(H) Inhibitory responses to bending the spinal cord were abolished by a combination of strychnine (5 μM) and GABAzine (10 μM) (*p < 0.05, n = 5 cells from 5 fish).
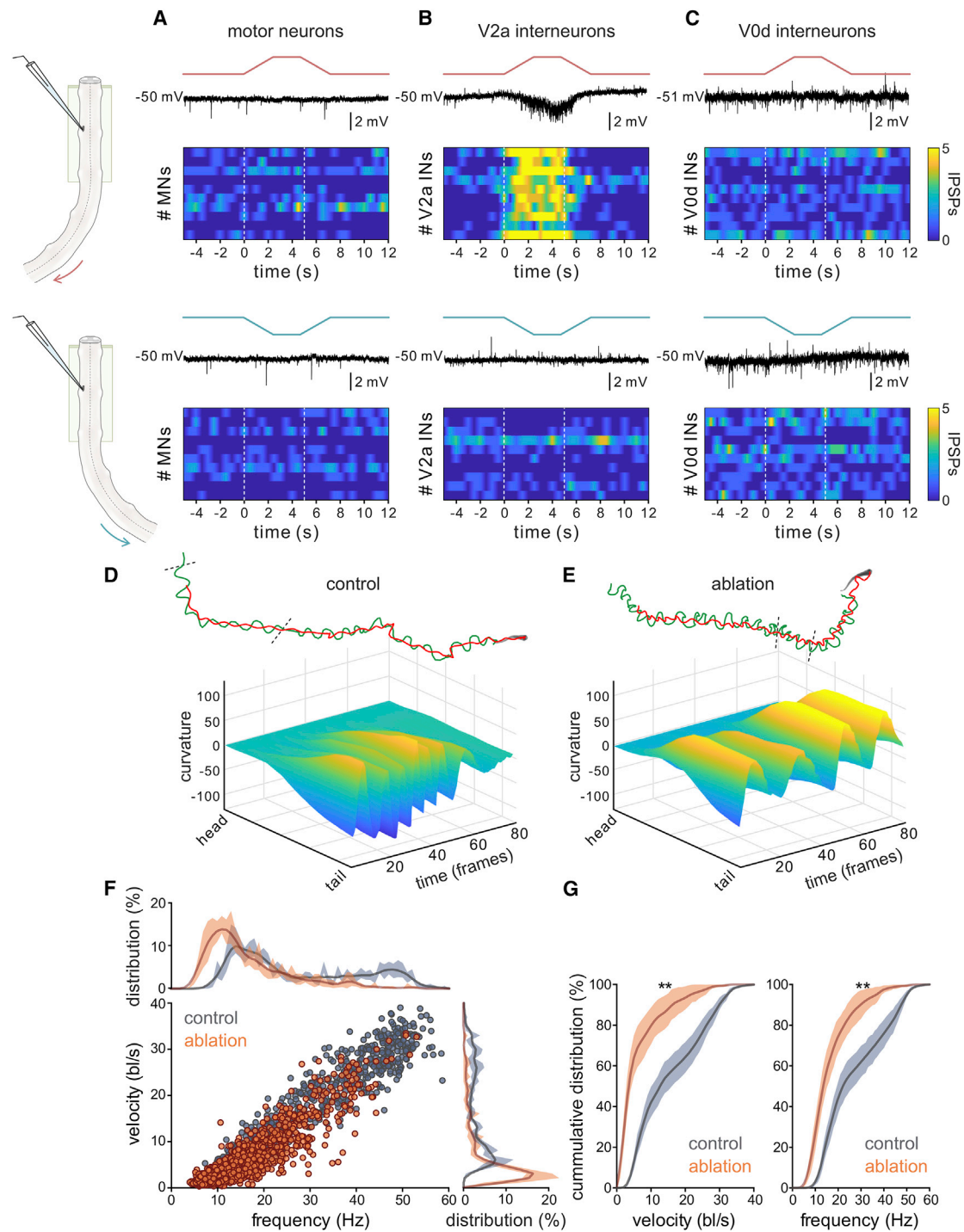
Figure 7. ILP neurons selectively inhibit the rhythm-generating circuit for efficient locomotion

(A) Bending the spinal cord in either direction had no effect on motor neurons recorded rostral to the bend (p > 0.05, n = 10 cells from 5 fish). Shown is a heatmap with each recording represented by each row, showing the number of IPSPs during spinal cord bending. Color represents the number of IPSPs binned in 500-ms windows. Shown above is a representative recording in current-clamp mode during the bend.

(B) Bending the spinal cord to stretch the contralateral spinal cord induced a significant IPSP response in V2a interneurons (****p < 0.0001, n = 10 cells from 5 fish), whereas bending in the opposite direction had no effect (p > 0.05, n = 10 cells from 5 fish).

(C) Bending the spinal cord in either direction had no effect on V0d interneurons (n = 10 cells from 6 fish).

(legend continued on next page)

A servomechanism for efficient locomotor behavior

Next we examined whether the movement-encoded inhibitory feedback signal from ILP neurons is integrated in the central locomotor network. Our analysis focused on three core components of the zebrafish locomotor network: motor neurons (Ampatzis et al., 2013; Gabriel et al., 2011; Song et al., 2016), rhythm-generating excitatory V2a interneurons (Ampatzis et al., 2014; Ausborn et al., 2012; Ljunggren et al., 2014; Eklöf-Ljunggren et al., 2012; Song et al., 2018, 2020), and left-right-coordinating inhibitory V0d interneurons (Satou et al., 2020), which were recorded during movement-induced activation of ILP neurons in the isolated spinal cord. In motor neurons, no response was induced by bending of the spinal cord in either direction (Figure 7A). In contrast, similar spinal cord movements elicited potent, reliable, and repeatable inhibition in rhythm-generating V2a interneurons (Figure 7B), whereas no responses were induced in coordinating commissural V0d interneurons (Figure 7C). Although we cannot completely rule out a contribution of other potential sensory systems that may also be activated by spinal cord bending, these results strongly suggest that ILP neurons exert powerful and selective inhibitory control over the rhythm-generating component of the locomotor circuit (Figure S5A).

Direct, movement-coupled inhibition of the rhythm-generating circuit could function to align rhythm generation with actual movement outcome for efficient locomotion. This was tested using selective ablation of ILP neurons combined with behavioral analysis. Compared with controls, zebrafish with ablated ILP neurons displayed less efficient swimming behavior (Figures 7D and 7E; Videos S2 and S3), characterized by a significant decrease in tail beat frequency and overall speed of swimming (Figures 7F, 7G, and S5C–S5E). Furthermore, in ablated animals, there was large variability in the amplitude of movements involving a broader rostrocaudal distribution in bending along their bodies at these low speeds (Figures 7E and S5B). In control animals, body bending was restricted to the caudal segments, except at higher swimming speeds (Figure S5B).

These results show that ILP neurons act with a dual function as proprioceptors and central commissural inhibitory neurons with direct and selective control over excitatory rhythm-generating neurons for efficient locomotion. The resulting circuit merges central generation of the locomotor rhythm with movement-driven proprioceptive feedback into a single hybrid network in the spinal cord.

DISCUSSION

Proprioception is essential for animal behavior, and its importance in motor control has long been recognized (Akay et al., 2014; Bässler and Büschges, 1998; Büschges et al., 2001, 2008, 2011; Grillner, 1975, 1985; Grillner and El Manira, 2020; Lam and Pearson, 2002; Mantziaris et al., 2020; Pearson, 1995, 2004; Rossignol et al., 2006; Tuthill and Azim, 2018). However, the complex interplay between peripheral proprioceptive feedback and central motor command circuits remains poorly understood. Furthermore, these two core components of movement have been largely considered as functionally and anatomically separate entities. In this study, we reveal a central proprioceptor organ that transforms local spinal cord tension at intervertebral joints into inhibitory feedback signals to form a unified circuit that elegantly couples motor command generation to movement.

Using a range of techniques, we demonstrate that intraspinal proprioceptors have a unique combination of gene expression, morphological features, and intrinsic properties that is reflective of their dual function as sensory neurons and as commissural inhibitory interneurons. They express mechanosensitive channels, such as Piezo2, that allow them to monitor the dynamics of spinal cord movement but also act as integrated inhibitory, commissural interneurons by providing direct and powerful inhibition of the rhythm-generating V2a population to align their activity with movement. These data reveal a central circuit resembling a servomechanism: V2a interneurons perform the role of an actuator, whose output is implemented by an effector (motor neurons) to generate body bending. The central proprioceptor organ provides rapid inhibitory feedback that scales with body bending, which, in turn, could counteract the output of the actuator with appropriate timing to terminate motor neuron drive. Recent modeling studies have shown that similar curvature-based proprioceptive feedback mechanisms that constrain body amplitudes are necessary to recapitulate fast and efficient locomotion (Gazzola et al., 2014, 2015; Gross et al., 2019), but until now, the biological basis for this mechanism has been unknown.

Intraspinal mechanosensitive neurons have been described previously in the most ancient vertebrate, the lamprey (Grillner et al., 1984). These neurons, called "edge cells," are distributed uniformly along their highly flexible spinal cord, which lacks support from a bony skeleton. However, it has been considered the only vertebrate that directly monitors movement of spinal cord tissue, with no such mechanisms demonstrated so far in species with a hard skeleton. We now show, using adult zebrafish, that intraspinal proprioceptors are distributed along the spinal cord at intervertebral sites where tension is focused in bony vertebrates. Furthermore, our results show that these specialized proprioceptor neurons express Piezo2 channels and detect spinal cord movement, and we reveal their developmental origins,

---

(D) Behavioral analysis showing the trajectory of a control zebrafish represented by the head (red line) and tail (green line) position over the period of swimming (600 frames, 2 s). Shown below is a 3D heatmap showing the angle of curvature across the body over time (80 frames, 266 ms, corresponding to the part of the trajectory delimited by the two dashed lines).

(E) The trajectory of swimming in a zebrafish in which ILP neurons were ablated (600 frames, 2 s), with a 3D heatmap below showing the angle of body curvature across the body over time (80 frames, 266 ms, corresponding to the part of the trajectory delimited by the two dashed lines). Ablated zebrafish showed a reduced frequency in their body bending with a more distributed curvature along the body.

(F) Plot of swim cycle frequency versus velocity across all cycles of swimming in control (n = 754 cycles from 11 fish) and ablated zebrafish (n = 1,699 cycles from 10 fish).

(G) Cumulative distribution of the velocity and frequency of swimming in control and ablated zebrafish. Ablated fish showed a significantly decreased swim velocity (**p < 0.01) and decreased cycle frequency (**p < 0.01).

Neuron
Article

CellPress
OPEN ACCESS

molecular profiles, connectivity, and behavioral function. ILP neurons also display small and weak membrane potential oscillations during fictive swimming, suggesting that they also receive synaptic input from the locomotor central pattern generator (CPG). This input is phase delayed relative to motor output, suggesting that it may derive from rostral V2a interneurons, and the timing of these inputs suggests that they may act to prime ILP neurons prior to their activation upon bending in each cycle. Similar phasic inputs have been shown in lamprey edge cells (Alford and Williams, 1987; Buchanan and Cohen, 1982; Buchanan and Kasicki, 1995; Vinay et al., 1996).

A separate sensory population known as cerebrospinal fluid-contacting neurons (CSF-c neurons or Kolmer-Agduhr cells) are local GABAergic neurons that project cilia into the CSF of the central canal (Barber et al., 1982; Dale et al., 1987; Vigh-Teichmann and Vigh, 1989). They have been shown recently, in lamprey and larval zebrafish, to monitor flow changes in CSF associated with body bending (Böhm et al., 2016; Jalalvand et al., 2016b) and detect activity-dependent changes in pH using Asic3 channels (Jalalvand et al., 2014, 2016a, 2016b). Although we cannot rule out a possible contribution of CSF-c neurons in adult zebrafish, in larval spinal circuits, these GABAergic neurons have been shown to project locally to target excitatory multipolar commissural descending (MCoD) interneurons, commissural primary ascending (CoPA) interneurons, and fast motor neurons and play a critical role in postural control during fast-speed locomotion (Böhm et al., 2016; Fidelin et al., 2015; Henderson et al., 2019; Hubbard et al., 2016). Additionally, Rohon-Beard (RB) neurons represent a transient population of intraspinal sensory neurons that innervate the skin during early life, before development of sensory neurons in dorsal root ganglia (Henderson et al., 2019; Li et al., 2003; Reyes et al., 2004; Roberts et al., 2012; Sillar and Roberts, 1988). In larval zebrafish, RB neurons have been shown to target the dorsal-most fast V2a interneurons in the spinal cord (Knafo et al., 2017). However, RB neurons are known to be excitatory and degenerate over the first few weeks of development (Reyes et al., 2004) and, therefore, are unlikely to mediate inhibition of V2a interneurons induced in adult zebrafish by spinal cord bending.

Our results in adult zebrafish now provide direct evidence of an organ of proprioception in the CNS. The constituent neurons are born from radial glia and cluster in each segment at the intervertebral discs, where tension is focused during movement. The mechanosensory neurons appear during a developmental period at the transition to adulthood, which coincides with degeneration of RB neurons, ossification of a bony skeleton, and transformation of muscle composition (Parichy et al., 2009; Reyes et al., 2004). Ossification of the vertebral column in zebrafish occurs in a rostral-to-caudal direction (Parichy et al., 2009); hence, it will be informative to examine the precise timing and rostrocaudal development of intraspinal proprioceptors in future studies.

Neurons that likely perform a similar role as spinal proprioceptors have been described anatomically in diverse vertebrate groups. So-called "outlier cells" were first reported in 1885 in the lateral white matter of the alligator spinal cord (Gaskell, 1885). Similar neurons have been subsequently identified in most vertebrates, among them reptiles, birds, and mammals, including humans, but their function remains unknown, although they are often noted for their resemblance to mechanosensory

neurons (Anadón et al., 1995; Anderson, 1963; Anderson et al., 1964; Donald, 1953; Fernández et al., 1998; Gaskell, 1885; Li et al., 2020; Necker, 2006; Schroeder and Egar, 1990; Schroeder, 1986; Sherrington, 1890). Given that it is known that the CNS is subject to changes in tension during normal body movements, combined with the existence of outlier white matter neurons directly at these sites of CNS distortion, it is highly likely that the mechanisms of central proprioception revealed in this study are widespread across vertebrates. A comprehensive evaluation of Piezo2 expression in the CNS will help address this question, and the results will likely have implications for disorders involving *piezo2* mutations (Alper, 2017) as well as for the important role of *piezo2* in normal skeletal development (Assaraf et al., 2020).

In summary, we identify a central organ of proprioception whose constituent mechanosensory neurons express Piezo2 and detect changes in tension in the spinal cord at the level of each intervertebral region. Intraspinal proprioceptors act as transducers of spinal cord movement and also as key commissural inhibitory interneurons with powerful and selective control over rhythm-generating V2a interneurons. These results reveal a novel hybrid circuit for sensorimotor integration in which the dynamics of spinal cord movement are coupled directly to the motor command network to align rhythm generation and actual motor outcome for efficient locomotion.

STAR★METHODS

Detailed methods are provided in the online version of this paper and include the following:

- KEY RESOURCES TABLE
- RESOURCE AVAILABILITY
  - Lead contact
  - Materials availability
  - Data and code availability
- EXPERIMENTAL MODEL AND SUBJECT DETAILS
  - Animals
- METHOD DETAILS
  - X-ray Computed Tomography (X-ray CT) scanning
  - Single-cell RNA sequencing
  - RNAscope assay
  - Patch-clamp electrophysiology
  - Immunohistochemistry
  - Mechanoclamp and mechanical stretch experiments
  - Whole spinal cord bending experiments
  - Behavioral analysis
- QUANTIFICATION AND STATISTICAL ANALYSIS

SUPPLEMENTAL INFORMATION

Supplemental Information can be found online at https://doi.org/10.1016/j.neuron.2021.01.018.

Neuron
Article

AUTHOR CONTRIBUTIONS

L.D.P. and A.E.M. conceived the project and designed the experiments. L.D.P. performed most of the experiments and analyses. M.B. performed immunohistochemical experiments and analyses and prepared patch-seq samples. I.P. performed RNA-seq data collection. P.F. performed analyses of the behavioral experiments. E.D. performed the RNAscope experiments. E.R.B. performed the initial experiments regarding the intrinsic properties of the neurons. F.I. performed CT scan data collection and analysis. P.R.S. provided access to the CT scanner. L.D.P. and A.E.M. prepared the figures and wrote the manuscript. All authors contributed to preparation of the figures and manuscript writing.

DECLARATION OF INTERESTS

The authors declare no competing interests.

REFERENCES

Akay, T., Tourtellotte, W.G., Arber, S., and Jessell, T.M. (2014). Degradation of mouse locomotor pattern in the absence of proprioceptive sensory feedback. Proc. Natl. Acad. Sci. USA *111*, 16877–16882.

Alford, S., and Williams, T.L. (1987). Inhibitory synaptic input to edge cells during fictive locomotion. Brain Res. *409*, 139–142.

Alper, S.L. (2017). Genetic Diseases of PIEZO1 and PIEZO2 Dysfunction. Curr. Top. Membr. *79*, 97–134.

Ampatzis, K., Song, J., Ausborn, J., and El Manira, A. (2013). Pattern of innervation and recruitment of different classes of motoneurons in adult zebrafish. J. Neurosci. *33*, 10875–10886.

Ampatzis, K., Song, J., Ausborn, J., and El Manira, A. (2014). Separate microcircuit modules of distinct v2a interneurons and motoneurons control the speed of locomotion. Neuron *83*, 934–943.

Anadón, R., Molist, P., Pombal, M.A., Rodríguez-Moldes, I., and Rodicio, M.C. (1995). Marginal cells in the spinal cord of four elasmobranchs (Torpedo marmorata, T. torpedo, Raja undulata and Scyliorhinus canicula): evidence for homology with lamprey intraspinal stretch receptor neurons. Eur. J. Neurosci. *7*, 934–943.

Anderson, F.D. (1963). The structure of a chronically isolated segment of the cat spinal cord. J. Comp. Neurol. *120*, 297–315.

Anderson, F.D., Meadows, I., and Chambers, M.M. (1964). The nucleus marginalis of the mammalian spinal cord. Observations on the spinal cord of cat and man. J. Comp. Neurol. *123*, 97–109.

Arber, S., and Costa, R.M. (2018). Connecting neuronal circuits for movement. Science *360*, 1403–1404.

Assaraf, E., Blecher, R., Heinemann-Yerushalmi, L., Krief, S., Carmel Vinestock, R., Biton, I.E., Brumfeld, V., Rotkopf, R., Avisar, E., Agar, G., and Zelzer, E. (2020). Piezo2 expressed in proprioceptive neurons is essential for skeletal integrity. Nat. Commun. *11*, 3168.

Ausborn, J., Mahmood, R., and El Manira, A. (2012). Decoding the rules of recruitment of excitatory interneurons in the adult zebrafish locomotor network. Proc. Natl. Acad. Sci. USA *109*, E3631–E3639.

Barber, R.P., Vaughn, J.E., and Roberts, E. (1982). The cytoarchitecture of GABAergic neurons in rat spinal cord. Brain Res. *238*, 305–328.

Bässler, U., and Büschges, A. (1998). Pattern generation for stick insect walking movements–multisensory control of a locomotor program. Brain Res. Brain Res. Rev. *27*, 65–88.

Berg, E.M., Bertuzzi, M., and Ampatzis, K. (2018). Complementary expression of calcium binding proteins delineates the functional organization of the locomotor network. Brain Struct. Funct. *223*, 2181–2196.

Björnfors, E.R., and El Manira, A. (2016). Functional diversity of excitatory commissural interneurons in adult zebrafish. eLife *5*, e18579.

Böhm, U.L., Prendergast, A., Djenoune, L., Nunes Figueiredo, S., Gomez, J., Stokes, C., Kaiser, S., Suster, M., Kawakami, K., Charpentier, M., et al. (2016). CSF-contacting neurons regulate locomotion by relaying mechanical stimuli to spinal circuits. Nat. Commun. *7*, 10866.

Breig, A. (1960). Biomechanics of the central nervous system: some basic normal and pathologic phenomena (Almqvist & Wiksell).

Brownstone, R.M., and Bui, T.V. (2010). Spinal interneurons providing input to the final common path during locomotion. Prog. Brain Res. *187*, 81–95.

Brownstone, R.M., and Wilson, J.M. (2008). Strategies for delineating spinal locomotor rhythm-generating networks and the possible role of Hb9 interneurones in rhythmogenesis. Brain Res. Brain Res. Rev. *57*, 64–76.

Buchanan, J.T., and Cohen, A.H. (1982). Activities of identified interneurons, motoneurons, and muscle fibers during fictive swimming in the lamprey and effects of reticulospinal and dorsal cell stimulation. J. Neurophysiol. *47*, 948–960.

Buchanan, J.T., and Kasicki, S. (1995). Activities of spinal neurons during brain stem-dependent fictive swimming in lamprey. J. Neurophysiol. *73*, 80–87.

Büschges, A., Schmidt, J., and Wolf, H. (2001). Sensory processing in invertebrate motor systems. eLS. Published online March 22, 2002. https://doi.org/10.1038/npg.els.0003638.

Büschges, A., Akay, T., Gabriel, J.P., and Schmidt, J. (2008). Organizing network action for locomotion: insights from studying insect walking. Brain Res. Brain Res. Rev. *57*, 162–171.

Büschges, A., Scholz, H., and El Manira, A. (2011). New moves in motor control. Curr. Biol. *21*, R513–R524.

Cadwell, C.R., Palasantza, A., Jiang, X., Berens, P., Deng, Q., Yilmaz, M., Reimer, J., Shen, S., Bethge, M., Tolias, K.F., et al. (2016). Electrophysiological, transcriptomic and morphologic profiling of single neurons using Patch-seq. Nat. Biotechnol. *34*, 199–203.

Cadwell, C.R., Scala, F., Li, S., Livrizzi, G., Shen, S., Sandberg, R., Jiang, X., and Tolias, A.S. (2017). Multimodal profiling of single-cell morphology, electrophysiology, and gene expression using Patch-seq. Nat. Protoc. *12*, 2531–2553.

Ceylan, D., Tatarlı, N., Abdullaev, T., Şeker, A., Yıldız, S.D., Keleş, E., Konya, D., Bayri, Y., Kiliç, T., and Çavdar, S. (2012). The denticulate ligament: anatomical properties, functional and clinical significance. Acta Neurochir. (Wien) *154*, 1229–1234.

Chen, Z., Gore, B.B., Long, H., Ma, L., and Tessier-Lavigne, M. (2008). Alternative splicing of the Robo3 axon guidance receptor governs the midline switch from attraction to repulsion. Neuron *58*, 325–332.

Coste, B., Mathur, J., Schmidt, M., Earley, T.J., Ranade, S., Petrus, M.J., Dubin, A.E., and Patapoutian, A. (2010). Piezo1 and Piezo2 are essential components of distinct mechanically activated cation channels. Science *330*, 55–60.

Coste, B., Xiao, B., Santos, J.S., Syeda, R., Grandl, J., Spencer, K.S., Kim, S.E., Schmidt, M., Mathur, J., Dubin, A.E., et al. (2012). Piezo proteins are pore-forming subunits of mechanically activated channels. Nature *483*, 176–181.

Dale, N., Roberts, A., Ottersen, O.P., and Storm-Mathisen, J. (1987). The morphology and distribution of 'Kolmer-Agduhr cells', a class of cerebrospinal-fluid-contacting neurons revealed in the frog embryo spinal cord by GABA immunocytochemistry. Proc. R. Soc. Lond. B Biol. Sci. *232*, 193–203.

Di Prisco, G.V., Wallén, P., and Grillner, S. (1990). Synaptic effects of intraspinal stretch receptor neurons mediating movement-related feedback during locomotion. Brain Res. *530*, 161–166.

Ding, Y., Vanselow, D.J., Yakovlev, M.A., Katz, S.R., Lin, A.Y., Clark, D.P., Vargas, P., Xin, X., Copper, J.E., Canfield, V.A., et al. (2019). Computational

Neuron
Article

3D histological phenotyping of whole zebrafish by X-ray histotomography. eLife 8, e44898.

Dobin, A., Davis, C.A., Schlesinger, F., Drenkow, J., Zaleski, C., Jha, S., Batut, P., Chaisson, M., and Gingeras, T.R. (2013). STAR: ultrafast universal RNA-seq aligner. Bioinformatics 29, 15–21.

Donald, D. (1953). On the incidence and locations of nerve cells in the spinal white matter of two species of primates, man and the cynomolgus monkey. J. Comp. Neurol. 99, 103–115.

Eklöf-Ljunggren, E., Haupt, S., Ausborn, J., Dehnisch, I., Uhlén, P., Higashijima, S., and El Manira, A. (2012). Origin of excitation underlying locomotion in the spinal circuit of zebrafish. Proc. Natl. Acad. Sci. USA 109, 5511–5516.

Faucherre, A., Nargeot, J., Mangoni, M.E., and Jopling, C. (2013). piezo2b regulates vertebrate light touch response. J. Neurosci. 33, 17089–17094.

Fernández, A., Radmilovich, M., and Trujillo-Cenóz, O. (1998). The marginal nuclei of the spinal cord in turtles: neuron assemblies in which γ-aminobutyric acid and nitric oxide synthase are colocalized. Exp. Brain Res. 122, 128–130.

Fidelin, K., Djenoune, L., Stokes, C., Prendergast, A., Gomez, J., Baradel, A., Del Bene, F., and Wyart, C. (2015). State-dependent modulation of locomotion by GABAergic spinal sensory neurons. Curr. Biol. 25, 3035–3047.

Finak, G., McDavid, A., Yajima, M., Deng, J., Gersuk, V., Shalek, A.K., Slichter, C.K., Miller, H.W., McElrath, M.J., Prlic, M., et al. (2015). MAST: a flexible statistical framework for assessing transcriptional changes and characterizing heterogeneity in single-cell RNA sequencing data. Genome Biol. 16, 278.

Friocourt, F., and Chédotal, A. (2017). The Robo3 receptor, a key player in the development, evolution, and function of commissural systems. Dev. Neurobiol. 77, 876–890.

Fuzik, J., Zeisel, A., Máté, Z., Calvigioni, D., Yanagawa, Y., Szabó, G., Linnarsson, S., and Harkany, T. (2016). Integration of electrophysiological recordings with single-cell RNA-seq data identifies neuronal subtypes. Nat. Biotechnol. 34, 175–183.

Gabriel, J.P., Mahmood, R., Kyriakatos, A., Söll, I., Hauptmann, G., Calabrese, R.L., and El Manira, A. (2009). Serotonergic modulation of locomotion in zebrafish: endogenous release and synaptic mechanisms. J. Neurosci. 29, 10387–10395.

Gabriel, J.P., Ausborn, J., Ampatzis, K., Mahmood, R., Eklöf-Ljunggren, E., and El Manira, A. (2011). Principles governing recruitment of motoneurons during swimming in zebrafish. Nat. Neurosci. 14, 93–99.

Gaskell, W. (1885). On a segmental group of ganglion cells in the spinal cord of the alligator. J. Physiol. 7, 19–30.

Gazzola, M., Argentina, M., and Mahadevan, L. (2014). Scaling macroscopic aquatic locomotion. Nat. Phys. 10, 758–761.

Gazzola, M., Argentina, M., and Mahadevan, L. (2015). Gait and speed selection in slender inertial swimmers. Proc. Natl. Acad. Sci. USA 112, 3874–3879.

Girdhar, K., Gruebele, M., and Chemla, Y.R. (2015). The behavioral space of zebrafish locomotion and its neural network analog. PLoS ONE 10, e0128668.

Goulding, M. (2009). Circuits controlling vertebrate locomotion: moving in a new direction. Nat. Rev. Neurosci. 10, 507–518.

Grillner, S. (1975). Locomotion in vertebrates: central mechanisms and reflex interaction. Physiol. Rev. 55, 247–304.

Grillner, S. (1985). Neurobiological bases of rhythmic motor acts in vertebrates. Science 228, 143–149.

Grillner, S. (1986). Interaction between sensory signals and the central networks controlling locomotion in lamprey, dogfish and cat. In Neurobiology of vertebrate locomotion, S. Grillner, P.S.G. Stein, D.G. Stuart, H. Forssberg, and R.M. Herman, eds. (Springer), pp. 505–512.

Grillner, S., and El Manira, A. (2020). Current principles of motor control, with special reference to vertebrate locomotion. Physiol. Rev. 100, 271–320.

Grillner, S., and Wallén, P. (1982). On peripheral control mechanisms acting on the central pattern generators for swimming in the dogfish. J. Exp. Biol. 98, 1–22.

Grillner, S., Williams, T., and Lagerbäck, P.-A. (1984). The edge cell, a possible intraspinal mechanoreceptor. Science 223, 500–503.

Grizzi, F., Chiriva-Internati, M., Franceschini, B., Bumm, K., Colombo, P., Ciccarelli, M., Donetti, E., Gagliano, N., Hermonat, P.L., Bright, R.K., et al. (2004). Sperm protein 17 is expressed in human somatic ciliated epithelia. J. Histochem. Cytochem. 52, 549–554.

Gross, D., Roux, Y., and Argentina, M. (2019). Curvature-based, time delayed feedback as a means for self-propelled swimming. J. Fluids Structures 86, 124–134.

Gulyás, M., Bencsik, N., Pusztai, S., Liliom, H., and Schlett, K. (2016). AnimalTracker: an ImageJ-based tracking API to create a customized behaviour analyser program. Neuroinformatics 14, 479–481.

Hao, J., and Delmas, P. (2011). Recording of mechanosensitive currents using piezoelectrically driven mechanostimulator. Nat. Protoc. 6, 979–990.

Hao, J., Padilla, F., Dandonneau, M., Lavebratt, C., Lesage, F., Noël, J., and Delmas, P. (2013). Kv1.1 channels act as mechanical brake in the senses of touch and pain. Neuron 77, 899–914.

Harrison, D.E., Cailliet, R., Harrison, D.D., Troyanovich, S.J., and Harrison, S.O. (1999). A review of biomechanics of the central nervous system–part II: spinal cord strains from postural loads. J. Manipulative Physiol. Ther. 22, 322–332.

Henderson, K.W., Menelaou, E., and Hale, M.E. (2019). Sensory neurons in the spinal cord of zebrafish and their local connectivity. Curr. Opin. Physiol. 8, 136–140.

Hubbard, J.M., Böhm, U.L., Prendergast, A., Tseng, P.B., Newman, M., Stokes, C., and Wyart, C. (2016). Intraspinal sensory neurons provide powerful inhibition to motor circuits ensuring postural control during locomotion. Curr. Biol. 26, 2841–2853.

Hunter, J.D. (2007). Matplotlib: A 2D graphics environment. Comput. Sci. Eng. 9, 90–95.

Jalalvand, E., Robertson, B., Wallén, P., Hill, R.H., and Grillner, S. (2014). Laterally projecting cerebrospinal fluid-contacting cells in the lamprey spinal cord are of two distinct types. J. Comp. Neurol. 522, 1753–1768.

Jalalvand, E., Robertson, B., Tostivint, H., Wallén, P., and Grillner, S. (2016a). The spinal cord has an intrinsic system for the control of pH. Curr. Biol. 26, 1346–1351.

Jalalvand, E., Robertson, B., Wallén, P., and Grillner, S. (2016b). Ciliated neurons lining the central canal sense both fluid movement and pH through ASIC3. Nat. Commun. 7, 10002.

Kiehn, O. (2016). Decoding the organization of spinal circuits that control locomotion. Nat. Rev. Neurosci. 17, 224–238.

Kimura, Y., Okamura, Y., and Higashijima, S. (2006). alx, a zebrafish homolog of Chx10, marks ipsilateral descending excitatory interneurons that participate in the regulation of spinal locomotor circuits. J. Neurosci. 26, 5684–5697.

Kiselev, V.Y., Yiu, A., and Hemberg, M. (2018). scmap: projection of single-cell RNA-seq data across data sets. Nat. Methods 15, 359–362.

Knafo, S., Fidelin, K., Prendergast, A., Tseng, P.B., Parrin, A., Dickey, C., Böhm, U.L., Figueiredo, S.N., Thouvenin, O., Pascal-Moussellard, H., and Wyart, C. (2017). Mechanosensory neurons control the timing of spinal microcircuit selection during locomotion. eLife 6, e25260.

Kucenas, S., Takada, N., Park, H.-C., Woodruff, E., Broadie, K., and Appel, B. (2008). CNS-derived glia ensheath peripheral nerves and mediate motor root development. Nat. Neurosci. 11, 143–151.

Kyriakatos, A., Mahmood, R., Ausborn, J., Porres, C.P., Büschges, A., and El Manira, A. (2011). Initiation of locomotion in adult zebrafish. J. Neurosci. 31, 8422–8431.

Lam, T., and Pearson, K.G. (2002). The role of proprioceptive feedback in the regulation and adaptation of locomotor activity. Adv. Exp. Med. Biol. 508, 343–355.

Lange, C., Rost, F., Machate, A., Reinhardt, S., Lesche, M., Weber, A., Kuscha, V., Dahl, A., Rulands, S., and Brand, M. (2020). Single cell sequencing of radial glia progeny reveals the diversity of newborn neurons in the adult zebrafish brain. Development 147, dev185595.

Li, W.-C., Soffe, S.R., and Roberts, A. (2003). The spinal interneurons and properties of glutamatergic synapses in a primitive vertebrate cutaneous flexion reflex. J. Neurosci. 23, 9068–9077.

Li, Y., Hou, W., Jia, Y., Wen, X., Rao, C., Xu, X., Wei, Z., Bai, L., and Tan, H. (2020). Pial surface CSF-contacting texture, subpial and funicular plexus in the thoracic spinal cord in monkey: NADPH diaphorase histological configuration. bioRxiv. https://doi.org/10.1101/2020.01.30.927509.

Ljunggren, E.E., Haupt, S., Ausborn, J., Ampatzis, K., and El Manira, A. (2014). Optogenetic activation of excitatory premotor interneurons is sufficient to generate coordinated locomotor activity in larval zebrafish. J. Neurosci. *34*, 134–139.

Mantziaris, C., Bockemühl, T., and Büschges, A. (2020). Central pattern generating networks in insect locomotion. Dev. Neurobiol. *80*, 16–30.

McCarthy, D.J., Campbell, K.R., Lun, A.T., and Wills, Q.F. (2017). Scater: preprocessing, quality control, normalization and visualization of single-cell RNA-seq data in R. Bioinformatics *33*, 1179–1186.

McClellan, A.D., and Sigvardt, K.A. (1988). Features of entrainment of spinal pattern generators for locomotor activity in the lamprey spinal cord. J. Neurosci. *8*, 133–145.

McLean, D.L., Fan, J., Higashijima, S., Hale, M.E., and Fetcho, J.R. (2007). A topographic map of recruitment in spinal cord. Nature *446*, 71–75.

Murthy, S.E., Dubin, A.E., and Patapoutian, A. (2017). Piezos thrive under pressure: mechanically activated ion channels in health and disease. Nat. Rev. Mol. Cell Biol. *18*, 771–783.

Murthy, S.E., Dubin, A.E., Whitwam, T., Jojoa-Cruz, S., Cahalan, S.M., Mousavi, S.A.R., Ward, A.B., and Patapoutian, A. (2018). OSCA/TMEM63 are an evolutionarily conserved family of mechanically activated ion channels. eLife *7*, e41844.

Necker, R. (2006). Specializations in the lumbosacral vertebral canal and spinal cord of birds: evidence of a function as a sense organ which is involved in the control of walking. J. Comp. Physiol. A Neuroethol. Sens. Neural Behav. Physiol. *192*, 439–448.

Nichterwitz, S., Chen, G., Aguila Benitez, J., Yilmaz, M., Storvall, H., Cao, M., Sandberg, R., Deng, Q., and Hedlund, E. (2016). Laser capture microscopy coupled with Smart-seq2 for precise spatial transcriptomic profiling. Nat. Commun. *7*, 12139.

Orlovsky, T., Orlovskiĭ, G.N., Deliagina, T., and Grillner, S. (1999). Neuronal control of locomotion: from mollusc to man (Oxford University Press).

Parichy, D.M., Elizondo, M.R., Mills, M.G., Gordon, T.N., and Engeszer, R.E. (2009). Normal table of postembryonic zebrafish development: staging by externally visible anatomy of the living fish. Dev. Dyn. *238*, 2975–3015.

Park, H.C., Shin, J., Roberts, R.K., and Appel, B. (2007). An olig2 reporter gene marks oligodendrocyte precursors in the postembryonic spinal cord of zebrafish. Dev. Dyn. *236*, 3402–3407.

Pearson, K.G. (1995). Proprioceptive regulation of locomotion. Curr. Opin. Neurobiol. *5*, 786–791.

Pearson, K.G. (2004). Generating the walking gait: role of sensory feedback. Prog. Brain Res. *143*, 123–129.

Picelli, S., Björklund, Å.K., Faridani, O.R., Sagasser, S., Winberg, G., and Sandberg, R. (2013). Smart-seq2 for sensitive full-length transcriptome profiling in single cells. Nat. Methods *10*, 1096–1098.

Picelli, S., Faridani, O.R., Björklund, Å.K., Winberg, G., Sagasser, S., and Sandberg, R. (2014). Full-length RNA-seq from single cells using Smart-seq2. Nat. Protoc. *9*, 171–181.

Pujala, A., and Koyama, M. (2019). Chronology-based architecture of descending circuits that underlie the development of locomotor repertoire after birth. eLife *8*, e42135.

R Core Team (2019). R: A language and environment for statistical computing (R Foundation for Statistical Computing).

Ramsköld, D., Wang, E.T., Burge, C.B., and Sandberg, R. (2009). An abundance of ubiquitously expressed genes revealed by tissue transcriptome sequence data. PLoS Comput. Biol. *5*, e1000598.

Ranade, S.S., Syeda, R., and Patapoutian, A. (2015). Mechanically activated ion channels. Neuron *87*, 1162–1179.

Reyes, R., Haendel, M., Grant, D., Melancon, E., and Eisen, J.S. (2004). Slow degeneration of zebrafish Rohon-Beard neurons during programmed cell death. Dev. Dyn. *229*, 30–41.

Roberts, A., Li, W.C., and Soffe, S.R. (2012). A functional scaffold of CNS neurons for the vertebrates: the developing Xenopus laevis spinal cord. Dev. Neurobiol. *72*, 575–584.

Rossignol, S., Dubuc, R., and Gossard, J.-P. (2006). Dynamic sensorimotor interactions in locomotion. Physiol. Rev. *86*, 89–154.

Rossitti, S. (1993). Biomechanics of the pons-cord tract and its enveloping structures: an overview. Acta Neurochir. (Wien) *124*, 144–152.

Sabatier, C., Plump, A.S., Le Ma, Brose, K., Tamada, A., Murakami, F., Lee, E.Y., and Tessier-Lavigne, M. (2004). The divergent Robo family protein rig-1/Robo3 is a negative regulator of slit responsiveness required for midline crossing by commissural axons. Cell *117*, 157–169.

Satou, C., Kimura, Y., and Higashijima, S. (2012). Generation of multiple classes of V0 neurons in zebrafish spinal cord: progenitor heterogeneity and temporal control of neuronal diversity. J. Neurosci. *32*, 1771–1783.

Satou, C., Sugioka, T., Uemura, Y., Shimazaki, T., Zmarz, P., Kimura, Y., and Higashijima, S.-i. (2020). Functional diversity of glycinergic commissural inhibitory neurons in larval zebrafish. Cell Rep. *30*, 3036–3050.e4.

Schroeder, D.M. (1986). The marginal nuclei in the spinal cord of reptiles: intraspinal mechanoreceptors. The Ohio Journal of Science *86*, 69–72.

Schroeder, D.M., and Egar, M.W. (1990). Marginal neurons in the urodele spinal cord and the associated denticulate ligaments. J. Comp. Neurol. *301*, 93–103.

Sherrington, C.S. (1890). II. On out-lying nerve-cells in the mammalian spinal-cord. Philos. Trans. R. Soc. Lond. B Biol. Sci. *181*, 33–48.

Sillar, K.T., and Roberts, A. (1988). A neuronal mechanism for sensory gating during locomotion in a vertebrate. Nature *331*, 262–265.

Song, J., Ampatzis, K., Björnfors, E.R., and El Manira, A. (2016). Motor neurons control locomotor circuit function retrogradely via gap junctions. Nature *529*, 399–402.

Song, J., Dahlberg, E., and El Manira, A. (2018). V2a interneuron diversity tailors spinal circuit organization to control the vigor of locomotor movements. Nat. Commun. *9*, 3370.

Song, J., Pallucchi, I., Ausborn, J., Ampatzis, K., Bertuzzi, M., Fontanel, P., Picton, L.D., and El Manira, A. (2020). Multiple Rhythm-Generating Circuits Act in Tandem with Pacemaker Properties to Control the Start and Speed of Locomotion. Neuron *105*, 1048–1061.e4.

Stephan, A.B., Tobochnik, S., Dibattista, M., Wall, C.M., Reisert, J., and Zhao, H. (2011). The Na(+)/Ca(2+) exchanger NCKX4 governs termination and adaptation of the mammalian olfactory response. Nat. Neurosci. *15*, 131–137.

Stil, A., and Drapeau, P. (2016). Neuronal labeling patterns in the spinal cord of adult transgenic Zebrafish. Dev. Neurobiol. *76*, 642–660.

Stuart, T., Butler, A., Hoffman, P., Hafemeister, C., Papalexi, E., Mauck, W.M., III, Hao, Y., Stoeckius, M., Smibert, P., and Satija, R. (2019). Comprehensive integration of single-cell data. Cell *177*, 1888–1902.e21.

Tuthill, J.C., and Azim, E. (2018). Proprioception. Curr. Biol. *28*, R194–R203.

Vigh-Teichmann, I., and Vigh, B. (1989). The cerebrospinal fluid-contacting neuron: a peculiar cell type of the central nervous system. Immunocytochemical aspects. Arch. Histol. Cytol. *52* (*Suppl*), 195–207.

Vinay, L., Barthe, J.Y., and Grillner, S. (1996). Central modulation of stretch receptor neurons during fictive locomotion in lamprey. J. Neurophysiol. *76*, 1224–1235.

Woo, S.-H., Lukacs, V., de Nooij, J.C., Zaytseva, D., Criddle, C.R., Francisco, A., Jessell, T.M., Wilkinson, K.A., and Patapoutian, A. (2015). Piezo2 is the principal mechanotransduction channel for proprioception. Nat. Neurosci. *18*, 1756–1762.

STAR★METHODS

KEY RESOURCES TABLE

REAGENT or RESOURCE	SOURCE	IDENTIFIER
Antibodies		
Monoclonal anti-Calbindin D-28k	Swant	Cat# 300; RRID: AB_10000347
Rabbit policlonal anti-mCherry	Abcam	Cat# ab167453; RRID: AB_2571870
Chicken polyclonal anti-GFP	Abcam	Cat# ab13970; RRID: AB_300798
Donkey anti-Mouse IgG (H+L) Highly Cross-Adsorbed Secondary Antibody, Alexa Fluor 647	Thermo Fisher Scientific	Cat# A-31571; RRID: AB_162542
Donkey anti-Rabbit IgG (H+L) Highly Cross-Adsorbed Secondary Antibody, Alexa Fluor 568	Thermo Fisher Scientific	Cat# A10042; RRID: AB_2534017
Goat anti-Chicken IgY (H+L) Secondary Antibody, Alexa Fluor 488 conjugate	Invitrogen	Cat# A11039; RRID: AB_142924
Streptavidin, Alexa Fluor 647 conjugate	Thermo Fisher Scientific	Cat# S32357
Streptavidin, Alexa Fluor 488 conjugate	Thermo Fisher Scientific	Cat# S11223
Streptavidin, Alexa Fluor 555 conjugate	Thermo Fisher Scientific	Cat# S32355
Chemicals, peptides, and recombinant proteins		
Ethyl 3-aminobenzoate methanesulfonate (MS-222)	Sigma Aldrich	Cat# E10521
PBS – Phosphate-Buffered Saline (10X) pH 7.4	Invitrogen	Cat# AM9625
Vectashield Hard Set Antifade Mounting Medium	Vector Laboratories	Cat# H1400
DMEM/F-12, HEPES, no phenol red	Thermo Fisher Scientific	Cat# 11039021
Papain	Worthington-Biochem	Cat# LK003178
eBioscience DRAQ5	Thermo Fisher Scientific	Cat# 65-0880-92
Triton X-100	Sigma Aldrich	Cat# T9284
SUPERase●In RNase Inhibitor (20 U/μL)	Thermo Fisher Scientific	Cat# AM2694
Dr-piezo2b-201 RNAscope probe	Advanced Cell Diagnostics	RRID: SCR_012481. Custom made RNA probe targeting 2050-3169 of GenBank: CU179656.1
Richard-Allan Scientific Neg-50 Frozen Section Medium	Thermo Fisher Scientific	Cat# 6502
20% Paraformaldehyde (formaldehyde) aqueous solution EM grade	Electron Microscopy Sciences	Cat# 15713
Tween-20	Sigma Aldrich	Cat# P1379
Bovine Serum Albumine	Sigma Aldrich	Cat# A2153
Strychnine	Sigma Aldrich	Cat# S0532
Gabazine	Sigma Aldrich	Cat# SR-95531
ProLong Gold Antifade Mountant	Thermo Fisher Scientific	Cat# P10144
OCT Cryomount	Histolab	Cat# 45830
2-methylbutane	Sigma Aldrich	Cat# M32631
LR White Medium Grade Kit	VWR	Cat# 100503-454
Phosphotungstic acid solution	Sigma Aldrich	Cat# HT152
Critical commercial assays		
The RNAscope Multiplex Fluorescent v2 Assay	Advanced Cell Diagnostics	Cat# 323136
Experimental models: organisms/strains		
Danio rerio: Tg(dbx1b:Cre)	Satou et al., 2012	Higashijima lab
Danio rerio: Tg(glyt2:LOXP-DsRed-LOXP-GFP)	Satou et al., 2020	Higashijima lab
Danio rerio: Tg(glyt2:GFP)	McLean et al., 2007	Higashijima lab
Danio rerio: Tg(vglut2a:LOXP-DsRed-LOXP-GFP)	Satou et al., 2012	Higashijima lab

Continued

REAGENT or RESOURCE	SOURCE	IDENTIFIER
Danio rerio: Tg(vglut1hs:GFP)	N/A	Higashijima lab
Danio rerio: Tg(olig2:DsRed)	Kucenas et al., 2008	Göteborgs Universitet, Zetterberg Zebrafish lab
Software and algorithms		
XMReconstructor	Carl Zeiss Inc.	https://www.zeiss.com/corporate/int/home.html
IMARIS	Oxford Instruments	RRID: SCR_007370; https://imaris.oxinst.com
R Core Team, 2019	R Foundation for Statistical Computing, Vienna, Austria.	RRID: SCR_001905; https://www.R-project.org
pClamp	Molecular Devices	RRID: SCR_011323; https://www.moleculardevices.com/
Spike2	Cambridge Electronic Design	RRID: SCR_000903; https://ced.co.uk
MATLAB	MATLAB and Statistics Toolbox Release 2012b, The MathWorks, Inc., Natick, Massachusetts, United States.	RRID: SCR_001622; https://www.mathworks.com
ImageJ	N/A	RRID: SCR_003070; https://imagej.nih.gov/ij/
Python	Python Software Foundation	RRID: SCR_008394; https://www.python.org/
GraphPad Prism7	GraphPad Software	RRID: SCR_002798; https://www.graphpad.com

RESOURCE AVAILABILITY

Lead contact
Further information and requests for resources and reagents should be directed to and will be fulfilled by the Lead Contact, Abdel El Manira (abdel.elmanira@ki.se).

Materials availability
This study did not generate new unique reagents.

Data and code availability
All data are available in the main text or the supplementary materials and are available upon request.

EXPERIMENTAL MODEL AND SUBJECT DETAILS

Animals
All experiments were conducted using zebrafish (*Danio rerio*). Zebrafish were raised and maintained in a core facility at the Karolinska Institute according to established procedures. Experiments were conducted on either wild-type or genetically modified zebrafish ranging from 2 days post fertilization (dpf) with undetermined sex to adult (up to 10 weeks) of either sex. All experimental protocols were approved by the local Animal Research Ethical Committee, Stockholm and were performed in accordance with EU guidelines.

METHOD DETAILS

The experiments were not randomized, and the investigators were not blinded to allocation during experiments and outcome assessment.

X-ray Computed Tomography (X-ray CT) scanning
A fixation and staining protocol was adapted from Ding et al. (2019). Briefly, 8-week old zebrafish were rapidly and humanely killed using an overdose of MS-222 placed on ice. A small cut was then made in the dorsal side of the belly to allow access for fixative. Fish were fixed in 10% chilled neutral buffered formalin (NBF) and left at room temperature for ~24 hours. Control fish were fixed lying on their side in a straight orientation. Zebrafish to be imaged in a bent orientation were fixed in an agar-coated dish with supporting pins

Neuron
Article

CellPress
OPEN ACCESS

placed at the head and tail to keep the body in a lateral curved shape during tissue fixation. Following fixation, fish were washed extensively in PBS, partially dehydrated in ethanol (35%, 50%), then tissue was stained by placing samples in 0.3% phosphotungstic acid (PTA, Sigma) solution for 24 hours. Samples were then dehydrated using an ethanol series (90%, 95%, 100%), then placed in a 1:1 solution of 100% ethanol and LR white acrylic resin (VWR, supplied by Electron microscopy sciences) overnight at room temperature. Finally, the samples were transferred to 100% LR white resin for 2 hours, and then to fresh 100% LR white resin for 1 hour. For the final embedding phase, individual samples were placed in 100% LR white resin in closed Eppendorf tubes with a parafilm covering to prevent oxygen exposure, and then placed in an incubator at 65 degrees to allow for resin polymerization. For imaging, the resin-embedded samples were removed from the Eppendorf tubes and superglued to the tip of a metal pin which could then be clamped and rotated inside the CT scanner. Micro-CT imaging of the samples was performed using a ZEISS Xradia 520 Versa (Carl Zeiss Inc.). A source voltage of 80 kV was used for the sample. 2,401 projections were captured using a 20x magnification lens with an exposure time of 20 s per projection. The raw images were reconstructed with proprietary reconstruction software (XMReconstructor, Carl Zeiss Inc.) using a cone beam reconstruction algorithm. This resulted in an image series of ortho-slices containing data in all three planes (xy, xz, yz) with isotropic voxel size of 0.38 μm with camera binning 1. The images were then segmented manually using IMARIS software.

Single-cell RNA sequencing

Transgenic zebrafish labeling intraspinal proprioceptors and V0d interneurons were obtained by crossing *Tg(dbx1b:Cre)* and *Tg(glyt2:LOXP-DsRed-LOXP-GFP)* (Satou et al., 2012), referred to as *Tg(glyt2,dbx:GFP)*. Thirty-two 7-8 week old *Tg(glyt2,dbx:GFP)* zebrafish of either sex were anesthetized in MS-222 dissolved in a slush of extracellular solution and the spinal cords dissected out of the body. Intact isolated spinal cords were incubated in 1ml of DMEM/F-12 (Thermofisher, #11039021, osmolality adjusted to 280-280 osm) containing papain 10 U/ml (Worthington-biochem, # LK003178) on a heated shaker at 37°C for 15 min. The enzymatic reaction was terminated by adding 1 mL of DMEM/F-12 (280-290 osm). The tissue was then spun down at 300 g for 5 min at 4°C and then re-suspended in 0.5 mL of DMEM/F-12 (280-290 osm). Mechanical trituration was then performed using fire-polished Pasteur pipettes, the homogenized solution was then filtered through a cell strainer (40 μm). The nucleated cell dye DRAQ5 (0.2 μl/ml, Thermofisher, #65-0880-92) was added 20 minutes before fluorescence-activated cell sorting (FACS). GFP and DRAQ5 positive cells of each sample were FACS sorted into single wells containing a mild hypotonic lysis buffer (0.2% Triton X-100, 2 U/μl RNase inhibitor) in two 384-well plates, immediately placed on ice and stored at −80°C.

For patch-seq, individual anatomically identified intraspinal proprioceptors and control V0d interneurons were harvested for sequencing (Cadwell et al., 2016, 2017; Fuzik et al., 2016). Using 7-8 week old *Tg(glyt2,dbx:GFP)* zebrafish, individual GFP-positive neurons (either lateral proprioceptors or dorsomedial V0d interneurons) were approached while applying continuous positive air pressure using glass electrodes with a large tip (resistance 1-4 MΩ) containing a small amount of extracellular solution. Once a clear and continuous seal was made between the neuron and the electrode, positive pressure was turned off, causing the soma to enter the tip of the pipette. Occasionally, small amounts of debris entered the pipette, which was quickly and carefully ejected using gentle, mouth-applied positive pressure. Neurons which were not obtained intact and clean of debris were discarded. Once a clean soma was obtained, the electrode was removed from the setup and using a syringe and tubing the contents of the electrode was immediately ejected into an RNase/DNase-free PCR tube containing 3 μL of lysis buffer (0.2% Triton X-100, 2 U/μl RNase inhibitor). The samples were then immediately frozen at −80°C and stored until 50-60 cells were collected. All samples were then prepared for RNA-seq following the protocol described in Nichterwitz et al. (2016).

Single-cell RNA sequencing (scRNA-seq) was performed following the previously described Smart-seq2 protocol (Picelli et al., 2013, 2014) and was performed by the Eukaryotic Single Cell Facility at SciLifeLab, Stockholm.

Two 384-well plates were obtained for the FACS dataset, and a total of 51 cells for the patch-seq dataset. For both the patch-seq and the FACS datasets, the reads from each cell were mapped to the zebrafish reference genome "Danio_rerio, Ensembl, GRCz11" using STAR version 2.5.3a (Dobin et al., 2013). The resulting bam files were filtered to keep only uniquely mapped reads. Gene expression was measured by calculating reads per kilobase gene model and million mapped reads (RPKMs) using the rpkmforgenes.py script (Ramsköld et al., 2009).

All analysis was performed in R, using the Seurat (version 3.0.0; Stuart et al., 2019) and Scater (version 1.10.1; McCarthy et al., 2017) packages for single cell data analysis. From the FACS dataset, we excluded low-quality cells with more than 30% reads from mitochondrial genes, more than 30% spike-ins, or expressed fewer than 1000 or higher than 10000 features. From the patch-seq dataset, we excluded low-quality cells with more than 30% spike-ins and less than 0.5% reads from mitochondrial genes. In both datasets, spike-ins and mitochondrial genes were removed from the gene set, as well as genes with an average expression of less than 0.25 over all cells.

Following cell and features filtering, the FACS dataset contained a total of 550 cells and the patch-seq dataset contained 33 cells (22 intraspinal lateral proprioceptors and 11 control V0d interneurons). Separate analyses were conducted on the two datasets. All data were log normalized, and cell-to-cell variation in gene expression driven by the percentage of ribosomal gene content, feature and count abundance was regressed out using the ScaleData function. A set of the 2000 most variable genes was generated using the variance-stabilizing transformation (vst) method as implemented in Seurat. Principal component analysis was performed on the FACS dataset, and the top 8 principal components of the variable gene set were used for two-dimensional data visualization with the RunTSNE function and for graph-based clustering with the FindClusters function. Genes differentially expressed in each cluster

compared to all other clusters were identified using the MAST test implemented in the function FindMarkers (Finak et al., 2015). Only genes with a log fold change of at least 0.25 were included in the analysis, and the P value cutoff was set to p < 0.01. The same method was used for the patch-seq data to identify differentially expressed genes inV0d interneurons and proprioceptors. In this case, due to the low sample size we relied upon the non-adjusted p values to identify enriched genes. To compare datasets, all genes enriched in anatomically identified intraspinal proprioceptors and V0d interneurons were compared against the list of significantly enriched genes in each cluster to calculate the % overlap in gene enrichment with each cluster. Using a second method, each of the single cells obtained from the patch-seq method were assigned a $glyt2^{+}/dbx1b^{+}$ cluster identity using the R package SCmap, a method to project individual cell gene profiles onto clustered datasets (Kiselev et al., 2018). The 500 most informative features and a similarity value of 0.5 was used for the assignment. The computations were performed on resources provided by SNIC through Uppsala Multidisciplinary Center for Advanced Computational Science (UPPMAX) under Project SNIC 2018/8-202.

RNAscope assay

For RNAscope analysis of *piezo2* expression a custom probe was designed (Dr-piezo2b-201). Spinal cords from 4 zebrafish (7-8 week old) were dissected out and fixed with 4% paraformaldehyde in PBS for 24h at room temperature. The samples were prepared for cryosectioning by immersion in 20% sucrose in PBS over night at 4°C, followed by 30% sucrose in PBS over night at 4°C, embedded in Neg-50 medium and frozen. Horizontal or sagittal sections (14 μm) were cut using a cryostat and collected on Superfrost Plus slides. The RNAscope Multiplex Fluorescent v2 Assay (Advanced Cell Diagnostics) was performed according to manufacturer's instructions with a few modifications. In brief, sections were air-dried for 60 min, washed in PBS for 5 min, incubated in Target Retrieval Buffer (heated to boiling point and then kept in a steamer) for 5 min, washed for 2 min with MilliQ water and dehydrated for 2 min in 100% ethanol at room temperature. The following incubations were then performed in the HyBEZ II oven at 40°C, with wash steps in between of 2x1 min washing buffer on a shaker: Protease III (20 m), C1 (Piezo2) and C2 (eGFP) -Probes (2 h), AMP 1 (30 min), AMP 2 (30 min), AMP 3 (15 min), HRP-C1 (15 min), TSA Plus Cy5 (Perkin Elmer, 30 min), HRP blocker (15 min), HRP-C2 (15 min), TSA Plus Fluorescein (Perkin Elmer, 30 min), HRP blocker (15 min). Sections were incubated with DAPI at room temperature before mounting with ProLong Gold Antifade Mountant (ThermoFisher Scientific). Sections were imaged using a laser scanning confocal microscope (LSM800, Zeiss) with a 40x or 63x water objective. For analysis, only intact slices in a straight orientation were used and neurons were classified as positive for GFP or *piezo2* if they had at least 5 RNA clusters at the soma. V0d interneurons and intraspinal proprioceptors were identified based on their respective positions in the spinal cord. For a subset of cells, the position of the GFP-positive neuron was obtained based on the relative position of the cell and section in the spinal cord.

RNAscope analysis in whole-mount 2 dpf zebrafish was performed according to the manufacturer's instructions (ACD Technical Note MK 50-016/Rev A/Date 10182017) with a few modifications. In brief, embryos were dechorionated using forceps at 2 dpf and fixed in 10% formaldehyde (in PBS) prepared fresh from EM grade formaldehyde ampules (EMS, cat no 15713), for 22 hours at room temperature. Samples were then washed in PBS containing 0.1% Tween-20 (PBST) for 10 min, followed by a dehydration series in 25, 50, 75 and 100% methanol (in PBST) for 10 min each at room temperature, and then stored in 100% methanol at −20°C for 3 days. Endogenous horse radish peroxidase activity was blocked by incubating samples in 0.2 M HCl in methanol for 30 min at room temperature. Samples were rehydrated by a series of 75, 50 and 25% methanol in PBST for 10 min each, followed by incubation in PBST containing 1% Bovine Serum Albumin (BSA) for 10 min at room temperature. Samples were incubated in Target Retrieval solution for 15 min at 100°C using a dry bath, and then immediately transferred to PBST containing 1% BSA for 5 min, followed by 100% methanol for 5 min and again PBST containing 1% BSA for 5 min at room temperature. Using a water bath, samples were incubated with Protease Plus for 30 to 60 min at 40°C and then placed in Probe Diluent at room temperature, followed by incubation with C1 (Piezo2) and C2 (eGFP) probes for 2.5 h at 40°C after which the assay was paused over night with samples placed in 5x SSC. The next day the following incubations were performed using a water bath set at 40°C, with wash steps in between of 3 × 10 min washing buffer on shaker: AMP 1 (30 min), AMP 2 (30 min), AMP 3 (15 min), HRP-C1 (15 min), Opal 690 (Perkin Elmer, 30 min), HRP Blocker (15 min), HRP-C2 (15 min), Opal 520 (Perkin Elmer, 30 min), HRP Blocker (15 min). Samples were incubated with DAPI for 10 min at room temperature before mounting with ProLong Gold Antifade Mountant (ThermoFisher Scientific). Samples were then imaged using a laser scanning confocal microscope with a 40x water objective (LSM800, Zeiss).

Patch-clamp electrophysiology

Adult zebrafish (8-10 weeks old) of either sex were used in all electrophysiological experiments. They were first anaesthetized using MS-222 dissolved in frozen extracellular solution and then the brainstem and spinal cord (with attached vertebral column) were dissected out of the body. For paired recordings of contralateral intraspinal proprioceptors, the vertebral column was also carefully removed to provide access to both sides of the spinal cord, which was then embedded, ventral side up on the surface of low-melt agarose (1.5%) for stability. The dissected preparation was then transferred to a recording chamber maintained at room temperature (20-22 °C) that was continuously perfused with extracellular solution containing (in mM): 134 NaCl, 2.9 KCl, 2.1 CaCl2, 1.2 MgCl2, 10 HEPES and 10 glucose with pH 7.8 adjusted with NaOH and an osmolarity of ∼290 mOsm.

For targeted recordings, intraspinal proprioceptors and V0d interneurons were labeled in *Tg(glyt2,dbx:GFP)* zebrafish (Satou et al., 2012, 2020); V2a interneurons were labeled in *Tg(Chx10:GFP)* zebrafish (Ampatzis et al., 2014; Ausborn et al., 2012; Kimura et al., 2006; Song et al., 2018, 2020); and motor neurons were back-labeled by injecting dextran dye into the muscles (Ampatzis et al., 2013; Gabriel et al., 2009, 2011). All recordings were performed using the whole-cell patch-clamp technique. Patch-clamp

electrodes were filled with a solution containing (in mM): 120 K-gluconate, 5 KCl, 10 HEPES, 4 Mg2ATP, 0.3 Na4GTP, 10 Na-phosphocreatine with pH 7.4 adjusted with KOH and an osmolarity of 275 mOsm. Neurons were visualized using a fluorescence microscope (Axioskop FS Plus, Zeiss) equipped with IR-differential interference contrast (DIC) optics and a CCD camera (Hamamatsu, Japan). Intracellular patch-clamp electrodes were advanced into the spinal cord through the meninges using a motorized micromanipulator (Luigs & Neumann, Germany) while applying constant positive pressure. Recorded neurons were located in the mid-body region approximately between spinal segments 8 and 16. In experiments where swimming was initiated, several tail muscles were left intact during the dissection and an extracellular recording electrode was placed at an intermyotomal cleft to record ventral root output. An extracellular stimulation electrode was placed dorsally at the border between the brainstem and spinal cord to induce swimming-related activity (10 × 1ms pulses at 1 Hz) (Kyriakatos et al., 2011). Extracellular signals were amplified using a differential AC amplifier (A-M Systems) and filtered with low and high cut-off frequencies of 300 Hz and 1 kHz, respectively. Intracellular signals were amplified using a MultiClamp 700B amplifier (Molecular Devices, Sunnyvale, CA) and low-pass filtered at 10 kHz. Electrophysiological data was digitized at 10 or 20 kHz using a Digidata 1322A A/D converter (Molecular Devices) and acquired using pClamp software (Molecular Devices). For analysis of the phase of the membrane potential oscillation during fictive swimming, the midpoint timing of each rhythmic depolarization and ipsilateral EMG burst was calculated for each cycle. The phase value was calculated as the delay between the timing of the mid-depolarization and mid-EMG burst relative to cycle period. The phase values were compensated to account for the delay incurred by the fact that the intracellular recording sites were several segments rostral to the EMG recording site. A mean phase value was calculated for each neuron.

For connectivity experiments, we recorded from pairs of intraspinal proprioceptors on opposite sides of the spinal cord separated by 1-6 segments. Single and multiple current pulses (0.5-1 ms duration, 100-200 Hz trains) were used to elicit action potentials in each intraspinal proprioceptor while recording synaptic responses in the neuron on the opposite side, which was held at approximately −50 mV to reveal inhibitory responses. Inhibitory postsynaptic potentials (IPSPs) were blocked using bath application of a GABA$_A$ receptor antagonist (gabazine, 10 μM) and glycine receptor antagonist (strychnine, 5 μM).

The analysis of electrophysiological data was performed using Spike2 (Cambridge Electronic Design), Clampfit (Molecular Devices) and MATLAB software. For all paired recordings 60-200 consecutive sweeps were run and raw traces illustrate averages of sweeps with IPSP responses. The IPSP amplitude was calculated as the difference between baseline and peak.

Immunohistochemistry

In a subset of experiments, single intraspinal proprioceptors were passively filled with 0.25% neurobiotin for post hoc analysis of their morphology. Spinal cords with neurobiotin-filled neurons were dissected out and transferred into 4% PFA solution overnight at 4 °C. The tissue was then washed extensively in PBS then incubated in 0.5% PBS-Triton for 2-4 hours. Samples were then incubated in streptavidin conjugated to either Alexa Fluor 488 (1:500, Invitrogen), Alexa Fluor 555 (1:500, Invitrogen), or Alexa Fluor 647 (1:500, Invitrogen). Non-specific protein binding sites were blocked with 0.15% normal goat serum and 1% Triton X-100 in PBS. Samples were mounted on coverslips using anti-fade fluorescent mounting medium (Vectashield Hard Set, Vector Labs). Whole-mount imaging of the spinal cords was acquired using a laser scanning confocal microscope (Zeiss LSM 800-airy or LSM 700). For overview image of an intraspinal proprioceptor neuron in Figure 2I, two consecutive orthogonal projections were stitched using Zeiss Zen microscope software. The neuronal processes (axons and dendrites) of labeled neurons were traced and reconstructed using Adobe Illustrator.

For analysis of GFP expression in *Tg(glyt2:GFP)* (McLean et al., 2007), *Tg(vglut2:LOXP-DsRed-LOXP-GFP)* (Björnfors and El Manira, 2016; Satou et al., 2012), *Tg(vglut1:GFP)* and *Tg(glyt2,dbx:GFP)* transgenic zebrafish, fish were first anesthetized in MS-222 and the spinal cords were dissected out and fixed in 4% PFA overnight at 4 °C. The spinal cords were washed five times for 5 min in phosphate buffer saline (0.01M PBS; pH = 7.4). Non-specific protein binding sites were blocked with 3% BSA and 2% normal donkey serum and 1% triton-100 in PBS for 30 min at room temperature. Spinal cords were then incubated with chicken anti-GFP (Abcam, ab13970) in 1% Triton X-100 in PBS at 4 °C for 72 h. After washing in PBS, the tissue was incubated with anti-chicken Alexa Fluor 488 antibody (Life Technologies, A11039) at 1:500 dilution overnight at 4 °C and subsequently rinsed in PBS and mounted using anti-fade fluorescent mounting medium (Vectashield Hard Set, Vector Labs). The number and position of neurons was identified from images taken with a laser scanning confocal microscope (LSM800, Zeiss), using a 40x water objective. Graphs were prepared with python using plotting libraries Matplotlib version 3.0.3 (Hunter, 2007) and Seaborn version 0.9.0 (https://github.com/mwaskom/seaborn). The position of neurons from approximately 15 segments from 4 fish was plotted for each transgenic line.

For the analysis of the dome structure, we performed Calbindin staining on *Tg(glyt2,dbx:GFP)* fish and Olig2 staining on *Tg(olig2:DsRed)* (Kucenas et al., 2008) fish. The immunohistochemistry was performed as described above, by using respectively the primary antibodies mouse anti-Calbindin (1:2000, CB D-28 k, Swant, #300) and rabbit anti-mCherry (1:1000, Abcam, ab167453) and the secondary antibodies anti-mouse Alexa Fluor 647 (1:500, Life Technologies, A31571) and anti-rabbit Alexa Fluor 568 (1:500, Life Technologies, A10042). For overview images of repeated dome structures in Figure 2B, nine consecutive orthogonal projections of the ventral spinal cord were stitched using Photomerge function in Adobe Photoshop.

For analysis of mCherry expression in *Tg(dbx1b:Cre)*, where Cre recombinase corresponds to a fusion protein of Cre-mCherry-NLS (nuclear localization signal; Satou et al., 2012), the spinal cords were dissected out and fixed in 4% PFA overnight at 4 °C. Then the tissues were cryoprotected overnight in 30% (w/v) sucrose in PBS at 4 °C, embedded in OCT Cryomount (Histolab), rapidly frozen in dry-ice-cooled isopentane (2-methylbutane; Sigma) at approximately −35 °C, and stored at −80 °C until use. Transverse

coronal plane cryosections (thickness 25 μm) of the tissue were collected and processed for immunohistochemistry as described for the whole mount preparations, by using the primary antibody rabbit anti-mCherry (1:1000, Abcam, ab167453) and the secondary antibody anti-rabbit Alexa Fluor 568 (1:500, Life Technologies, A10042). Images were taken with a laser scanning confocal microscope (LSM800, Zeiss), using a 40X water objective.

Mechanoclamp and mechanical stretch experiments

For mechano-clamp experiments we adapted a protocol from Hao and Delmas (2011) for use in an intact spinal cord preparation. Intraspinal proprioceptors were approached in the isolated spinal cord using a patch-clamp recording electrode and a second electrode with a heat-polished, blunt ending with approximate diameter 1-3 μm. The probe was positioned at an angle of approximately 40 degrees to the preparation, manipulated into the spinal cord and slowly moved toward the neuron so it was just touching the surface of the soma. When in place, a patch-clamp recording was made of the neuron using the recording electrode. The blunt probe was then used to generate rapid and brief indentations of the soma using an MM3a micromanipulator system driven by a piezoelectric motor (Kleindiek Nanotechnik, Reutlingen, Germany). The velocity, intensity and duration of the mechanical stimulus was controlled using nanocontrol software (NC5.8) and a nanocontrol unit (Kleindiek Nanotechnik, Germany). The probe was set to a speed of 1000 μ/s for a duration 500 ms, and the amplitude of stimulation increased in steps of 1 μm in a range of 1-10 μm. A 10 s gap was left between each stimulation. All recordings were performed in voltage clamp mode with neurons held at −65 mV. Recordings were discarded if we observed changes in access resistance, or there were changes in input resistance or holding current that did not recover to baseline after offset of the mechanical stimulus. The mechanical stimulation protocol was tested on non-proprioceptor control neurons in the spinal cord, but no currents were observed in response to any tested amplitude of mechanical stimulus.

Analysis was performed using Clampfit (Molecular Devices) software. The peak amplitude of mechanically-activated inward currents was measured for each stimulus. All responses showed a rapidly-inactivating and more slowly-inactivating component so traces were fitted in clampfit software with a double-exponential curve using the levenberg-marquat method to obtain a fast and a slow tau value, for the first and second current component, respectively. For pharmacological experiments, mechanically-activated inward currents were measured for repetitions of a 6 μm stimulus before and after bath application of ruthenium red (50 μM). Example recordings shown in the figure are averages of at least 3 sweeps for each stimulus amplitude.

For experiments in which a local region of lateral spinal cord tissue was stretched, a small tungsten wire attached to the end of a patch pipette was used to penetrate the spinal cord from the side at approximately 90 degrees to the preparation at the ventrolateral margin, approximately 0.5-1.5 segments away from an intraspinal proprioceptor. The mechanical stimulation was always placed so that it was not in direct contact with the intraspinal proprioceptor. A patch-clamp recording was then made from the proprioceptor in current-clamp mode. Using a motorized micromanipulator (Luigs & Neumann, Germany), the mechanical pipette was moved laterally to stretch the lateral projections of the neuron. The duration of the stimulus was 5 s and the velocity and amplitude of the stretch was systematically changed. To explore the effect of amplitude, the velocity was fixed at 15 μm/s and the amplitude set to either 5, 10 or 15 μm. To explore the effect of velocity, the amplitude was fixed at 10 μm and the velocity set to either 5, 10 or 15 μm/s. Recordings were discarded if we observed changes in access resistance during the mechanical stimulation or changes in membrane potential that did not return to baseline after offset of the mechanical stimulus. For analysis, we quantified the number of action potentials and the spike frequency within the first 1 s of the stimulus when stimulated from rest, while the peak voltage response measured when the neuron was held at −80 mV. The dendrite stretch protocol was tested on non-proprioceptor control neurons in the spinal cord which showed no responses to stretching the spinal cord.

Whole spinal cord bending experiments

Dissected spinal cords with the vertebral column removed were first embedded ventral side up on the surface of 1.5% low-melt agarose in the recording chamber. Using the tip of a scalpel, 5-10 segments of the caudal spinal cord were then released by carefully cutting away the surrounding agarose, while ensuring rostral segments remained stably embedded. After transferring to the patch-clamp setup, a small metal ring formed at the end of a tungsten wire attached to a motorized micromanipulator (Luigs & Neumann, Germany) was then placed around the free segments of spinal cord. The manipulator was aligned parallel with the spinal cord, allowing movements of the manipulator to the left or the right to cause spinal cord bending in the respective direction. Patch-clamp recordings were then made of a neuron (an intraspinal proprioceptor, V0d interneuron, motor neuron or V2a interneuron) in the embedded rostral segments, and postsynaptic inhibitory responses were recorded in response to bending of the spinal cord. Neurons were recorded between 3-10 segments away from the bent region of spinal cord. Recorded neurons were held at approximately −50 mV or −30 mV to reveal IPSP responses which were analyzed using MiniAnalysis (Synaptosoft). The number of IPSPs was binned into 500 ms time windows and plotted in MATLAB. Note that in V0d and motor neuron recordings in which no response to bending was observed, inhibitory responses were recorded in nearby proprioceptors or V2a interneurons in the same preparation, highlighting that a lack of a response was not due to an issue with preparation or bending protocol. For ablation experiments, the preparation was first embedded in agarose ventral side up, then 10-20 proprioceptors were ablated along one side of the spinal cord using a 2-photon microscope (Zeiss LMS 980, wavelength 910 nm). The caudal spinal cord was then freed to perform bending experiments while recording from a rostral, contralateral proprioceptor.

Neuron
Article

CellPress
OPEN ACCESS

Behavioral analysis

Tg(glyt2,dbx:GFP) zebrafish (n = 10 fish, 4-6-weeks old) were first anaesthetized in MS-222 and then embedded on their side in 1.5% low-melt agarose, and covered with fish water containing 0.03% MS-222. They were then placed under a 2-photon microscope (Zeiss LMS 510) and approximately 20-30 GFP-labeled intraspinal proprioceptors at the ventro-lateral edges were photoablated (wavelength 910 nm) along one side of the spinal cord. The zebrafish were then unembedded and re-embedded on their opposite side and the process was repeated, resulting in a total of 40-60 intraspinal proprioceptors ablated. Control animals (n = 11 fish) were anaesthetized and embedded in the same way as ablated animals but were not subjected to two-photon laser ablation. For the sham ablation group, 40-60 V0d interneurons were ablated across both sides of the spinal cord (n = 5 fish). The control, proprioceptor ablated, or sham ablated zebrafish were allowed to recover from anesthesia and acclimate in the recording chamber for 20 minutes before analyzing their swimming. For behavioral analysis, fish were placed in a circular glass dish (12 cm diameter) containing 60 mL of fish water, illuminated from below by an LED light box. Swimming was evoked by touching the caudal part of the body using a fine tungsten pin and recordings were performed at 300 frames per second (fps).

To quantify the fish velocity, the coordinates of the centroid of the fish were extracted using an ImageJ plugin, 'AnimalTracker' (Gulyás et al., 2016), and analyzed using MATLAB. To analyze the curvature of the body, recordings were processed using a custom MATLAB script based on the procedure developed and applied by Girdhar et al. (2015) and Pujala and Koyama (2019). First, the background image was calculated as the median of 5 frames obtained along the recording and subtracted from each frame. Frames were then binarized (black/white) using an adjusted threshold value to isolate the fish. The function 'bwmorph' was used on the binarized frame to extract the midline of the fish. In order to obtain a stable starting point of the fish midline, the centroid of the head was tracked using the function 'imfindcircles'. The coordinates were manually corrected using a graphic user interface (GUI) when needed. These midlines were then converted into a smoother curve to remove some pixel noise and then cubic splines were used to obtain 10 evenly spaced segments from the head to the tail. The curvature of the fish was computed as the sum of the angle differences between each segment. The total curvature along the time was used to identify the swimming half-cycle (peak-to-peak: representing the maximum bending of the body from one side to the other), to extract the amplitude (degrees) and the duration (frames). The data resolution was then increased by 100 and smoothed. Different exclusion criteria for frames were applied using specific threshold values or GUI. The first initial cycle in each swim episode was excluded, as well as cycles of swimming in which the fish was close to the edge of the dish, was turning or on its side, or if there was a specific error in tracking (e.g., detecting objects other than the fish). After manual validation, 1699 cycles for the proprioceptor ablated fish, 1005 cycles for the sham ablation fish, and 754 for the control fish were used for the analysis of the swimming. The mean velocity (bodylength/second), amplitude (degrees) and frequency (Hz) were quantified for each fish together with their distribution. The distribution was calculated using a binning interval of 1 Hz (frequency), 1 bodylength/second (velocity) and 10 degrees (amplitude).

QUANTIFICATION AND STATISTICAL ANALYSIS

Graphs and statistical analyses were made using GraphPad Prism software (https://www.graphpad.com/). A two-tailed Student's t test (two groups) or a one-way ANOVA with Tukey's post hoc multiple comparisons (> two groups) were performed as appropriate. Differences were considered to be significant if $p < 0.05$.

Supplemental Information

A spinal organ of proprioception

for integrated motor action feedback

Laurence D. Picton, Maria Bertuzzi, Irene Pallucchi, Pierre Fontanel, Elin Dahlberg, E. Rebecka Björnfors, Francesco Iacoviello, Paul R. Shearing, and Abdeljabbar El Manira
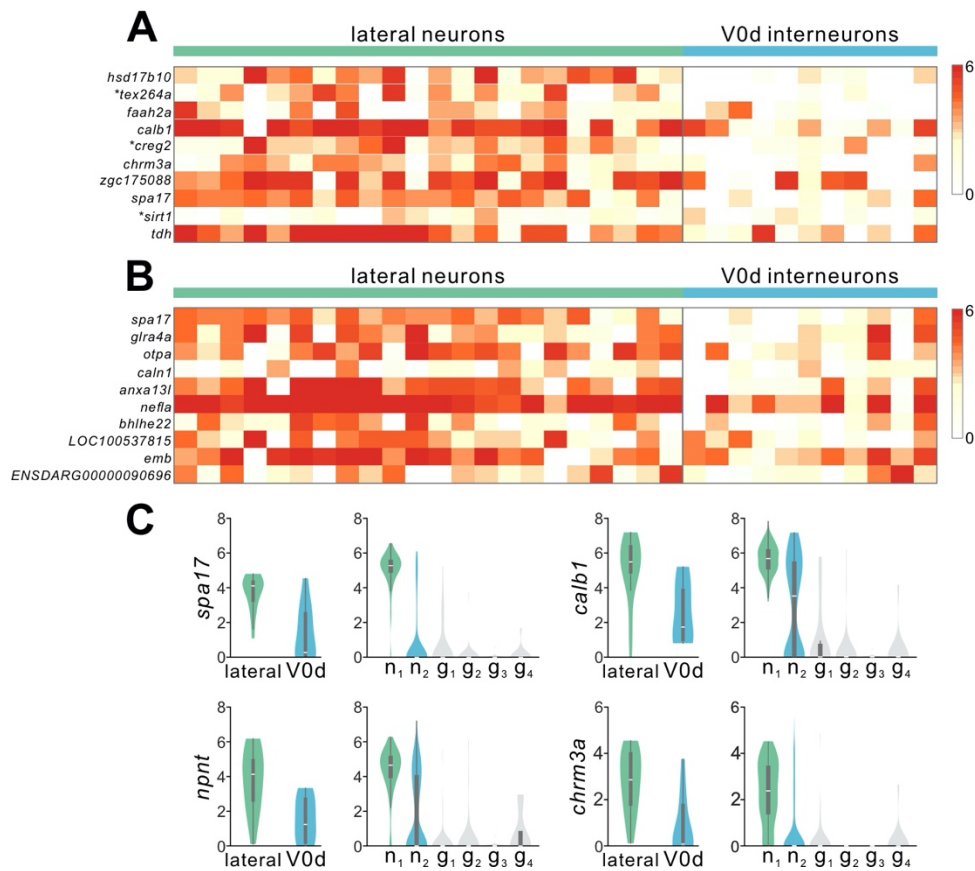
Figure S1 Shared enrichment of genes in single harvested lateral neurons and neuronal cluster 1 (n_1), Related to Figure 4

(A) Heatmap of the ten most enriched genes in individual anatomically identified lateral neurons and their relative expression in V0d interneurons. All but three (indicated by *) of the most enriched genes in lateral neurons were also significantly enriched in the $glyt2^+/dbx1b^+$ population cluster n_1.

(B) Heatmap of the ten most significantly enriched genes in $glyt2^+/dbx1b^+$ cluster n_1 and their expression levels in single anatomically identified lateral neurons and V0d interneurons.

(C) Violin plots of a range of genes enriched in lateral neurons that were also enriched in $glyt2^+/dbx1b^+$ cluster n_1.
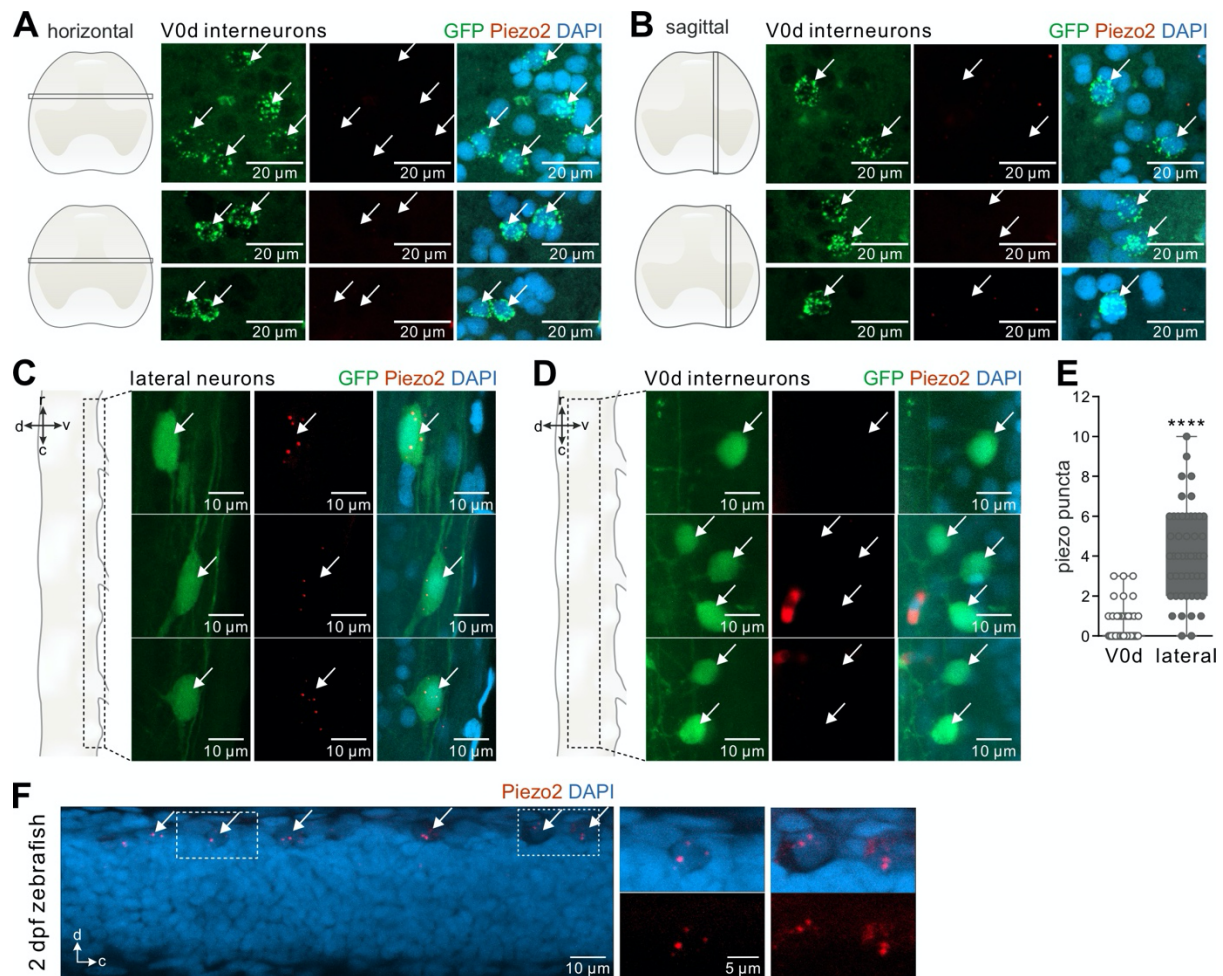
Figure S2 RNAscope analysis of *piezo2* expression in adult and embryonic zebrafish, Related to Figure 5

(A) Images from horizontal sections of spinal cord at the level of V0d interneurons following the RNAscope Multiplex Fluorescent Assay. V0d interneurons (white arrows) showed RNA puncta for GFP but lacked *piezo2* RNA puncta.

(B) Images from sagittal sections of spinal cord showing V0d interneurons lacking *piezo2* RNA puncta.

(C) Images of whole-mount spinal cords following RNAscope Multiplex Fluorescent Assay. ILP neurons at the ventrolateral spinal cord showed RNA puncta for *piezo2*.

(D) Images taken at the level of V0d interneurons, which showed none, or very few, RNA puncta for *piezo2*.

(E) ILP neurons had significantly higher levels of *piezo2* RNA puncta compared to V0d interneurons (****P <0.0001, n = 49 ILP neurons, n = 72 V0d neurons from 2 fish).

(F) Images of whole mount embryonic spinal cord (2dpf) following RNAscope Multiplex Fluorescent Assay. At this stage of development *piezo2* was restricted to Rohon-Beard sensory neurons (white arrows) with large somata at the dorsal edge of the spinal cord (n = 9 fish).
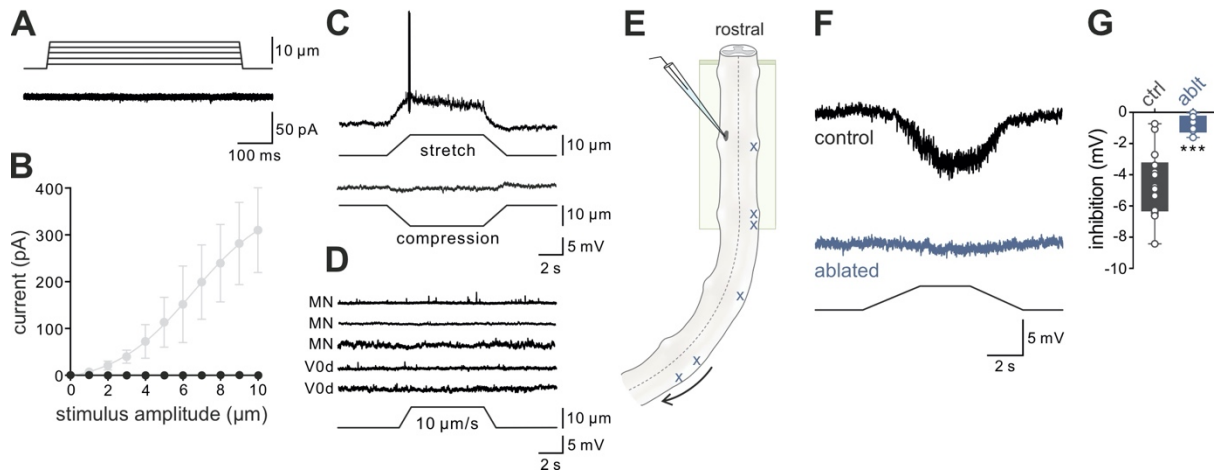
Figure S3 Lack of mechanosensation in motoneurons and V0d interneurons and effect of ILP neuron ablation on inhibitory responses to spinal cord bending, Related to Figures 5 and 6

(A) Voltage-clamp recording of a motoneuron showing a lack of mechanically activated (MA) currents in response to indentation of the soma in a range of 1 to 10 μm.

(B) MA currents were not observed in motoneurons (n = 2 cells from 2 fish) or V0d interneurons (n = 2 cells from 2 fish). The data points shown in grey illustrate the MA currents observed in ILP neurons.

(C) A current clamp recording of an ILP neuron showing activation in response to stretch of the spinal cord but not to compression.

(D) Current clamp recordings showing that neither motoneurons (n = 3 cells from 2 fish) nor V0d interneurons (n = 2 cells from 2 fish) responded to stretch of the spinal cord.

(E) Schematic showing spinal cord bending experiments in which ILP neurons were ablated along one side of the spinal cord.

(F) Current clamp recordings of an ILP neuron in response to bending of the spinal cord in control (black trace) and after ablation (blue trace) of contralateral ILP neurons.

(G) Pooled data showing a significant reduction in the inhibitory response to bending following ablation of contralateral ILP neurons (***p<0.001, control: n = 14 cells from 9 fish; ablation: n = 6 cells from 3 fish).
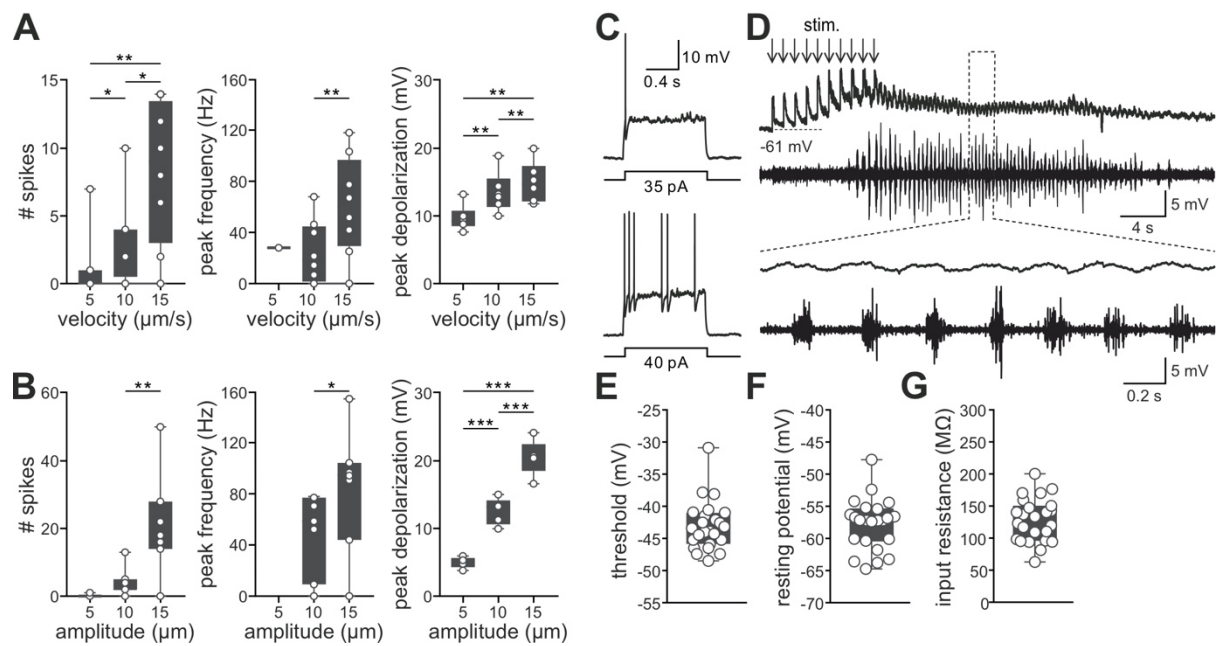
Figure S4 ILP neurons are low-threshold mechanoreceptor neurons coding the amplitude and velocity of spinal cord movements, Related to Figure 5

(A) Pooled data on the effect of local spinal cord organ stretch velocity on the responses of ILP neurons. An increase in the stretch velocity significantly increased the number of spikes (*$P<0.05$; **$p<0.01$; n = 8 cells from 4 fish), the frequency of spiking (**$p<0.01$, n = 8 cells from 4 fish) and amplitude of depolarization (**$p<0.01$, n = 6 cells from 4 fish).

(B) Pooled data on the effect of local spinal cord organ stretch velocity on the responses of ILP neurons. An increase in the stretch amplitude significantly increased the number of spikes (*$P<0.05$, n = 7 cells from 4 fish), frequency of spiking (*$p<0.05$, n = 7 cells from 4 fish) and amplitude of depolarization (***$p<0.001$, n = 5 cells from 3 fish).

(C) Responses of ILP neurons to depolarizing current injection.

(D) ILP neurons were not recruited during evoked fictive locomotion and displayed only small oscillations of their membrane potential (n = 5 cells from 5 fish).

(E) ILP neurons displayed a low threshold for action potentials (n = 24 cells).

(F) ILP neurons displayed a depolarized resting membrane potential (n = 24 cells).

(G) ILP neurons displayed a low input resistance (n = 24 cells).
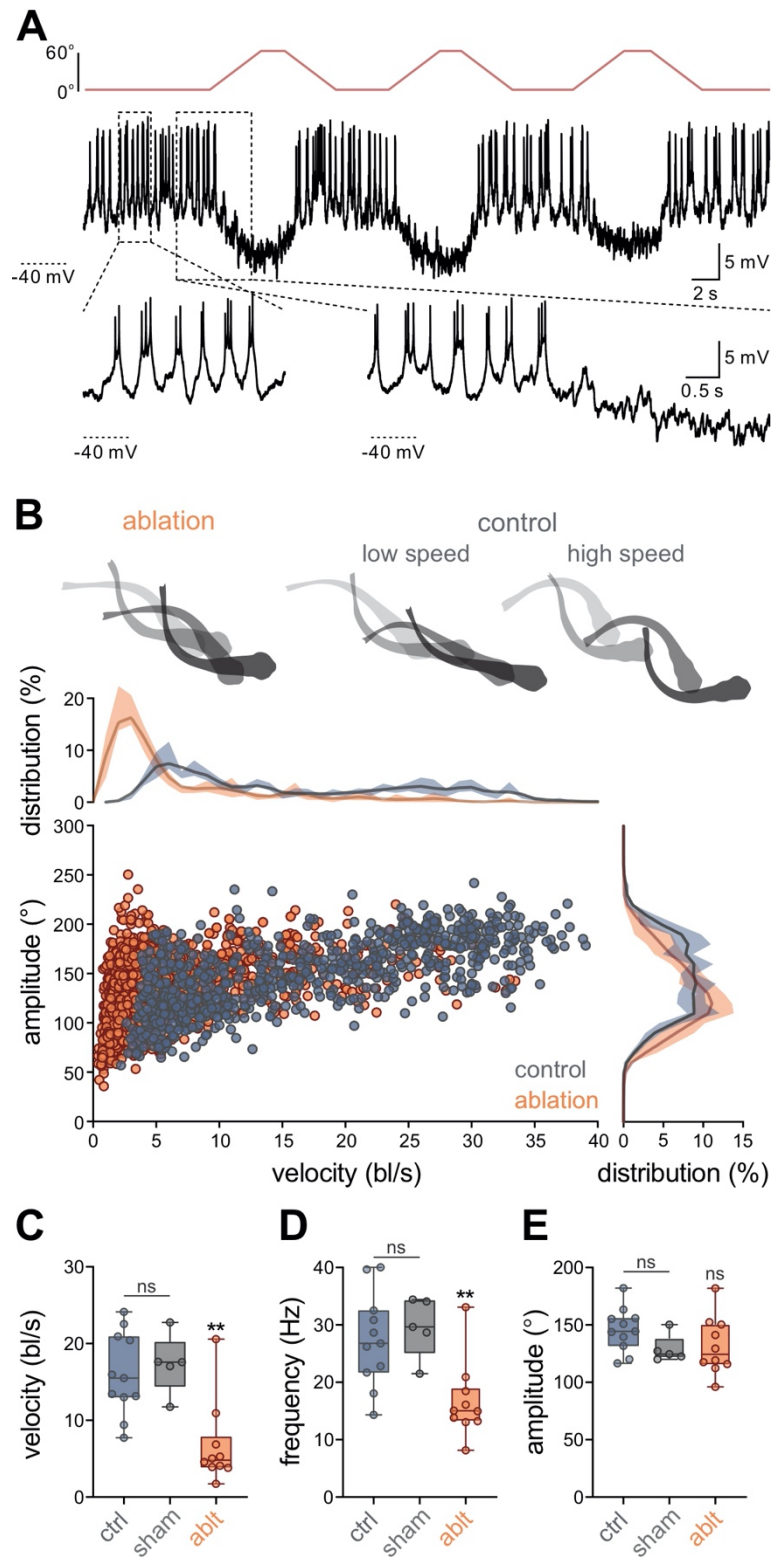
Figure S5 Movement-encoded suppression of firing in rhythm-generating V2a interneurons and effects on tail bend amplitude in ILP-ablated zebrafish, Related to Figure 7

(A) Raw trace showing a patch-clamp recording of a pacemaker, rhythm-generating V2a interneuron which was held depolarized using tonic current injection to induce repetitive bursts

of action potentials. The responses to three bends of caudal spinal cord are shown in which the pacemaker burst firing of the V2a interneuron is silenced.

(B) Images of fish outlines showing swimming in an ILP-ablated (slow) and control zebrafish (slow and fast swimming). During swimming, ablated fish show movement across the body, which is only seen in control fish at high speeds. Below shows a plot of swim velocity vs. body bend amplitude across all cycles of swimming in control (n = 754 cycles from 11 fish) and ILP-ablated zebrafish (n = 1699 cycles from 10 fish).

(C) Mean velocity values for individual control, sham ablated and proprioceptor ablated zebrafish (**p<0.01, n = 11 control, n = 5 sham ablation, n = 10 proprioceptor ablation).

(D) Mean swim frequency values for individual control, sham ablated and proprioceptor ablated zebrafish (**p<0.01, n = 11 control, n = 5 sham ablation, n = 10 proprioceptor ablation).

(E) Mean body amplitude values for individual control, sham ablated and proprioceptor ablated zebrafish (control: n = 11 control, n = 5 sham ablation, n = 10 proprioceptor ablation).